Experimental assessment of the similarity law for a heat conduction problem

A. Charaka, J. Berger, Rafik Belarbi

Experimental assessment of the similarity law for a heat conduction problem

Achraf Charaka[a,b*], Julien Berger[a], Rafik Belarbi[a,b]

June 27, 2022

[a] LaSIE, UMR 7356 CNRS La Rochelle Université, Avenue Michel Crépeau, 17042, La Rochelle Cedex1, France
[b] 4evLab, LaSIE, CNRS, EDF R&D, La Rochelle Université
*corresponding author, e-mail address : achraf.charaka@univ-lr.fr

Abstract

Similarities are mathematical laws, which are based on the dimensionless formulation of the governing equation of a physical phenomenon. Consequently, a set of characteristic dimensionless numbers is obtained. Similarities aim, via these numbers, to find equivalences between particular configurations. This approach is widely adopted, especially in fluid and aerodynamic problems. In the building context, the phenomena of heat and mass transfer in porous media occur with slow kinetics. Thus, similarities can be employed to reduce the duration of experimental campaigns to characterize material properties. These laws were investigated here in the case of a heat transfer problem through an experimental campaign. Two equivalent configurations were submitted to a heat stress. Temperatures inside materials were measured and compared to assess the validity of thermal similarity. A complete evaluation of uncertainty propagation was then carried out. Uncertainties related to the sensor position, its response time, the omission of mass transfer, the sensor systematic accuracy, the random measurement aspect, the one-dimensional transfer hypothesis and the boundary condition modeling were evaluated. The comparison of both configurations was carried out based on the confidence interval of both measurements. The results showed a good agreement between the reference and reduced experiment. On the basis of these findings, similarities were experimentally verified within a margin of discrepancy that was justified. Thus, they can be adopted in heat transfer experiments in order to identify equivalent configurations that are easier to conduct.

Keywords

Heat transfer, similarity analysis, porous material, experimental benchmarking, uncertainty quantification.

1 Introduction

In the building sector, energy consumption has increased continuously in the recent years, depleting natural resources and in turn increasing greenhouse gas emissions [1]. One option for addressing this is to focus on the envelope and building materials, reducing their environmental footprint and better controlling sensible and latent heat flows. Recently, new types of materials have been proposed in building sector. On the one hand, there are bio-based materials, which are generally based on the use of concrete with the partial substitution of a plant substance. They are good insulators and moisture regulators [2]. Studies conducted on this type of material have shown that it is a suitable alternative in terms of energy efficiency [3]. On the other hand, agricultural and industrial waste can also be used to form composite concretes. It has also been shown [4] that the manufacture of recycled concrete reduces CO_2 emissions by 58% compared to the production of clinker.

All such materials are porous media, composed of a solid matrix, a water liquid phase and a humid air phase. They have complex and heterogeneous micro-structures [5, 6]. With the presence of temperature and humidity variations induced by climatic conditions and building use, coupled heat and mass transfer phenomena [7] occur through the material. To accurately model these phenomena through porous building walls, it is necessary to determine the material properties of heat and mass transfer. In other words, experimental campaigns are required to characterize the materials. However, some procedures require a long period. For example, determining the adsorption and desorption curves of concrete can last several months. The classical method lies on the use of saturated saline solutions. A study of the adsorption curve [8] showed that it takes approximately five months for different concrete samples. Indeed, the water mass equilibrium at each relative humidity level is reached slowly. The `ProUmid` device is used in laboratories world-wide to determine the adsorption curve and examine the moisture adsorption behavior of materials. This dynamic vapor adsorption device employs the gravimetric method, assessing the mass variation of samples until it reaches a mass equilibrium. The test duration can range from three to six months, depending mainly on the micro-structure of a material and its porosity. The long duration of these kinds of tests is primarily due to the kinetics of heat and mass transfer phenomena. Indeed, water transport is slow [9]. The Fourier number $\mathrm{Fo}\,[-]$ is the parameter that describes the kinetics of transfer. Take for example a hemp concrete sample whose thickness is $L = 20\,\mathsf{cm}$. Considering that it undergoes a moisture stress during $t_0 = 10\,\mathsf{d}$ while remaining in the hygroscopic mode, the hemp concrete mass diffusivity is estimated at $D_0 = 1.06\,10^{-8}\,[\mathsf{m}^2.\mathsf{s}^{-1}]$ where $T = 20\,^{\circ}\mathsf{C}$. Thus, the typical experience duration is deduced $\tau = 43.6\,\mathsf{d}$. To overcome this problem, the similarity law can be employed to reduce the duration of experiments. By definition, similarities are mathematical laws which aim to find equivalences among several configurations. This method consists of the dimensionless formulation of the governing equations [10]. As a result, dimensionless characteristic numbers are obtained which are used to obtain equivalences.

The literature shows that similarity laws have been adopted in various scientific fields [11–13]. In acoustics, for example, it has been demonstrated that the sound analysis of two equivalent centrifugal fans was similar [14]. Another study [15] focused on the evaluation of the temperature of enclosed turbulent flames for different lengths. Analysis of the experimental results has shown that the behavior of temperatures, measured by means of an optical pyrometer, satisfies a similarity law. Similarities were also used in a study of structures [16] exposed to impacts with low and high velocity projectiles. It presented an experimental verification of these laws, using three different scales, three different materials and two loading cases. In addition, fluid dynamics constitutes a major field highlighting the use of these techniques [17–19]. In [20], an analysis was performed to study the fluid flow and heat transfer characteristics of the steady laminar natural convection boundary layer flow over a semi-infinite horizontal flat plate. This plate was subjected to a variable wall temperature. Similarity laws were used to identify the parameters governing the dynamic and thermal wall-fluid interaction. Within the same scientific field, other studies were carried out in order to evaluate the impact of certain physical parameters on the flow of particular fluids [21–23]. In this case, temperature, pressure gradient, velocity and shear stress were investigated by means of preliminary similarity analysis. For example, a study was conducted on a steady incompressible Williamson fluid flow [24]. Using appropriate similarity transformations, the authors converted a set of partial differential equations based on flow situations into a system of non-linear coupled ordinary differential equations. Thereby, the impact of some parameters, namely the one related to the Williamson fluid, was observed on some problem variables.

In the field of heat and mass transfer in buildings, these laws are applied for different purposes. A method for calculating the solution of the transfer equations has been described in [25]. A dimensionless formulation was suggested as an intermediate step. In addition, the advantages of using a dimensionless analysis by scaling the governing equations of heat and mass transfer were explored in [26]. It also permitted the definition of heat and mass kinetics, geometric and dynamic similarities among different physical materials. The dimensionless analysis of a heat and mass transfer model has also been addressed in [10]. The authors adopted this approach to estimate the mechanisms governing these transfers for a medium density fiberboard. This was achieved by assessing the magnitude of the dimensionless numbers of the model and their

response surface. An experimental method using a small-scale model for the building wall and similarity laws based on the governing equations of simultaneous heat and moisture transfer through porous media was presented in [27]. Converted values from the small-scale model were compared with the numerical results of the reference configuration, this comparison showed a good agreement. Apart from the application of such laws, it is worth noting that most studies used them to obtain equivalent theoretical configurations. Nevertheless, this approach requires an experimental campaign to compare the results between equivalent cases and evaluate the noticed discrepancies.

In general, it is easy to express theoretically the laws of similarity related to a physical problem, particularly the one concerning heat transfer in porous materials. In addition, these laws are based on several assumptions that can be modeled mathematically. As an example, the boundary conditions and the variation laws of material properties constitute two important hypotheses. Experimentally, it would not always be evident to respect entirely the defined assumptions. For example, a material property is supposed constant at the macroscopic scale. In reality, it varies in space following the micro-structure and pores distribution. Thus, two samples issued from a material do not have necessarily the same properties. In this context, it would be judicious to evaluate how far the experimental similarities are validated. Errors, that would arise from assumptions, can be discussed by means of a study of uncertainty. Many researches have proposed methodologies to compute uncertainties following two main approaches: probabilistic and deterministic. In the deterministic approach, uncertainty is defined as a scalar. In this case, the calculation is less costly but less accurate. On the other hand, uncertainty is evaluated more accurately in the probabilistic approach. However, this requires more data and computation time. For example, the authors in [28] focused on the analysis of experimental uncertainties related to the convective transfer coefficient h_c. They relied on random uncertainty in the measurements of air and wall temperatures. Through a differential calculation, they were able to express and evaluate the ratio of the relative uncertainty of h to the relative uncertainties of the measured temperatures. The viewpoint of the study is purely deterministic, and shows that the expressions obtained are in good agreement with the ones simulated via the Monte Carlo method. Based on their results, the ratio can be used as a continuous function to minimize the uncertainty on h_c for similar configurations. A second study [29] introduced a non-probabilistic interval process model to the characterization of time-varying parameter uncertainties. Two numerical methods referred to as the *Monte Carlo method under interval process model* and the *sensitivity analysis method under interval process model* were adopted simultaneously to predict the uncertain temperature. Furthermore, this method involved the use of a finite differences scheme for the estimation of temperature derivatives according to model parameters. Other authors have adopted the probabilistic approach. In [30], the work was based on a random aspect governing the input parameters of the model. Indeed, propagation of uncertainty through the physical model was investigated by solving two specific simple stochastic problems using the Non-Intrusive Spectral Projection method. The uncertain parameters were described by either a Gaussian or a Log-Normal probability distribution function. For each of the problems, the stochastic and the deterministic mean solutions were compared and the resulting confidence intervals were obtained. Similarly, a random aspect was taken into account in [31] to generate multiple model inputs. Moreover, a random collocation method and a modified random collocation method were advanced, based on spectral analysis theory. In both methods, the truncated high-order polynomial series were adopted to approximate temperature responses with respect to random parameters. The accuracy of the two methods was then tested using a traditional Monte Carlo simulation and two numerical examples.

In this work, we carry out an experimental assessment of similarity laws on a unidirectional heat transfer problem. Mass transfers will be neglected in this study. Indeed, the coupling of the two phenomena is less easy to control than a pure heat transfer model. The study provides also a detailed calculation of the uncertainties related to the hypothesis of the experimental tests and the accuracy of the used equipment. The uncertainty evaluation is essential to discuss the validity of heat transfer similarities. The study of uncertainties is of great importance. The numerical or experimental result is not conclusive and needs to be completed by using the associated confidence interval. This justifies the result and is obtained due to the

study of uncertainties. The paper is structured as follows. The next section defines the governing equations, the dimensionless formulation of the problem and the similarity law. Section 3 introduces the experimental facility to assess the heat transfer similarity. Section 4 contains a complete evaluation of the measurement uncertainty. Section 5 presents the results and discusses the validity of the similarity for two configurations. Section 6 concludes and suggests future works.

2 Methodology

2.1 Governing equations

First, the study case consists in defining the equation that describes the heat transfer in homogeneous media (superior in size that the representative elemental volume) [32], [33] with high porosity. In this work, the mathematical model considers temperature T [K] as a driving potential. It is based on the general heat equation, first developed by Joseph Fourier (1822). The problem is written as follows:

$$\rho\, c_q \frac{\partial T}{\partial t} = \nabla \cdot \left(k_q \nabla T \right). \tag{1}$$

In Eq. (1), three coefficients have been introduced. k_q [W.m^{-1}.K^{-1}] is the heat transfer coefficient and ρ [kg.m^{-3}] the material density. In addition, c_q [J.kg^{-1}.K^{-1}] is the heat storage coefficient. We define both material density and heat transfer coefficient as follows:

$$\rho = (1-n)\,\rho_s + n\,S_w\,\rho_w + n\,S_a\,\rho_a\,. \tag{2}$$

$$k_q = n\,k_{qw} + (1-n)\,k_{qs}\,. \tag{3}$$

Equation (2) expresses the density of a porous material according to the three phases solid, liquid and air [34], where n represents the porosity of the material, and ρ_s, ρ_w and ρ_a the density of solid phase, water and air respectively. S_w and S_a represent the degree of saturation in liquid water and the gas phase. Moreover, the work of Lagarde (1965) [35] expresses the heat transfer coefficient in Eq. (3) in terms of the porosity in a saturated porous media, where k_{qw} is the liquid water thermal conductivity and k_{qs} that of the solid matrix.

We present **Hypothesis 1**, which considers a one-dimensional transfer along the x-axis [36]. This is possible by insulating the facets parallel to the transfer direction. In these areas, thermal flux is negligible. Moreover, we neglect water mass transfers in our case. The impact of these on heat transfer is assumed therefore not considered. This will be the **Hypothesis 2** of our study [37]. For $x \in \Omega_x$ and $t \in \Omega_t$ where x is the first space coordinate, t the instant of the experiment. Eq. (1) can be simply reduced to:

$$\rho\, c_q \frac{\partial T}{\partial t} = \frac{\partial}{\partial x}\left(k_q \frac{\partial T}{\partial x} \right). \tag{4}$$

$\Omega_x = [0, L]$ is the space domain where x varies and $\Omega_t = [0, t_{\text{ref}}]$ the trial time interval. L and t_{ref} are the sample length and experiment duration respectively. At the initial state, the temperature is known :

$$T = T_0(x) \qquad \forall x \in \Omega_x\,. \tag{5}$$

where T_0 is a given function of space. At the material/air interface, the Robin condition is generally applied, where air temperature is known. In the case of a high ambient homogenization and a large air flow, we define the **Hypothesis 3**. It assumes that temperature at the interface is very close to that of air. Thus, we present the Dirichlet condition [38]:

$$T = T^{\infty}(t)\,, \qquad x = 0\,,\, t \in \Omega_t\,. \tag{6}$$

The temperature T^{∞} at the interface is a time function that represents the varying climatic stress. The other side of the material is insulated, meaning that the thermal flow is negligible, thus:

$$\frac{\partial T}{\partial x} = 0\,, \qquad x = L\,,\, t \in \Omega_t\,. \tag{7}$$

Furthermore, the assumption of a local thermal equilibrium is made, given the slow kinetics of the transfer and the predominance of diffusion effects compared to convection through the porous matrix [39]. Thus, the hypotheses of the model can be summarized as follows:

Hypothesis 1. *The heat transfer is one-dimensional.* ■

Hypothesis 2. *Mass transfer and latent effects are negligible.* ■

Hypothesis 3. *The boundary conditions are assumed to be of the* Dirichlet *type.* ■

Hypothesis 4. *The local thermal equilibrium is assumed.* ■

Next section is devoted to the study of the dimensionless heat transfer case. This step is important before discussing the notion of similarities. Indeed, the dimensionless formulation is an intermediate procedure which aims to define similarities, or equivalent configurations.

2.2 Dimensionless problem

The dimensionless formulation of an equation consists in describing its variables as constants corresponding to a particular case. This latter is defined by the researcher, and can represent the initial instant of an experiment. Dimensionless studies have been discussed in previous research [40]. More precisely, it has been applied to heat and mass transfer equations according to [26], [10] and [25]. The first step is to transform the spatial and temporal field into :

$$t^\star = \frac{t}{t_{\,\mathrm{ref}}}\,, \qquad x^\star = \frac{x}{L}\,. \tag{8}$$

Equation (8) introduces the dimensionless first space coordinate $x^\star$ and experiment instant $t^\star$. In parallel, temperature follows the same reasoning, and the reference value of this quantity can represent that of the material at its initial state:

$$u = \frac{T}{T_0}\,. \tag{9}$$

u represents the dimensionless temperature. On the other hand, the heat transfer k_q and thermal storage c_q coefficients change under the same formulation :

$$k_q^\star = \frac{k_q}{k_q^{\mathrm{ref}}}\,, \qquad \rho^\star = \frac{\rho}{\rho^{\mathrm{ref}}}\,, \quad c_q^\star = \frac{c_q}{c_q^{\mathrm{ref}}}\,. \tag{10}$$

Likewise, k_q^{ref}, c_q^{ref} and ρ^{ref} are the material heat transfer, heat storage coefficients and density respectively at $t = 0$. The substitution of the dimensionless quantity u and the coefficients $k_q^\star$, $c_q^\star$ and $\rho^\star$ in Eq. (4) enables us to obtain the new equality:

$$\rho^\star\, c_q^\star \frac{\partial u}{\partial t^\star} = \mathrm{Fo}_q \frac{\partial}{\partial x^\star}\left(k_q^\star \frac{\partial u}{\partial x^\star}\right). \tag{11}$$

Thus we observe the dimensionless Fourier number Fo appearing, and its expression is given as follows:

$$\mathrm{Fo}_q = \frac{k_q^{\mathrm{ref}}\, t_{\,\mathrm{ref}}}{\rho^{\mathrm{ref}}\, c_q^{\mathrm{ref}}\, L^2}\,. \tag{12}$$

Finally, the new boundary conditions for heat transfer are written as follows :

$$u = u^\infty(t^\star) \quad at \quad x^\star = 0\,, \qquad \frac{\partial u}{\partial x^\star} = 0 \quad at \quad x^\star = 1\,. \tag{13}$$

Where, u^∞ designates the dimensionless air temperature. Thus, the dimensionless formulation has built a new closed system, independent of time and space fields. It relies only on the number Fo_q. This transformation was introduced to ensure a transition to the laws of similarity. Indeed, equivalences would have to be determined using a basic configuration. Then, the transformation shown in this section, is used to operate on this configuration.

2.3 Similarity law

In practice, the laws of similarity are applied to a reference case. Their usefulness consists in obtaining configurations equivalent to our reference case [41]. They can minimize some difficulties related to the real case. In the context of heat transfer, we can use these laws to change the material while maintaining similarity of results [14] and [42]. The dimensions of the sample can also be changed. Since the transfer phenomena have a slow kinetic, the goal of the study is to reduce the duration of an experiment, while working on the same material. In heat transfer, kinetic describes the rate of heat diffusion within a material. In the building physics field, the Fourier number describes fully this notion. Fig. 1 highlights the process that defines these laws.

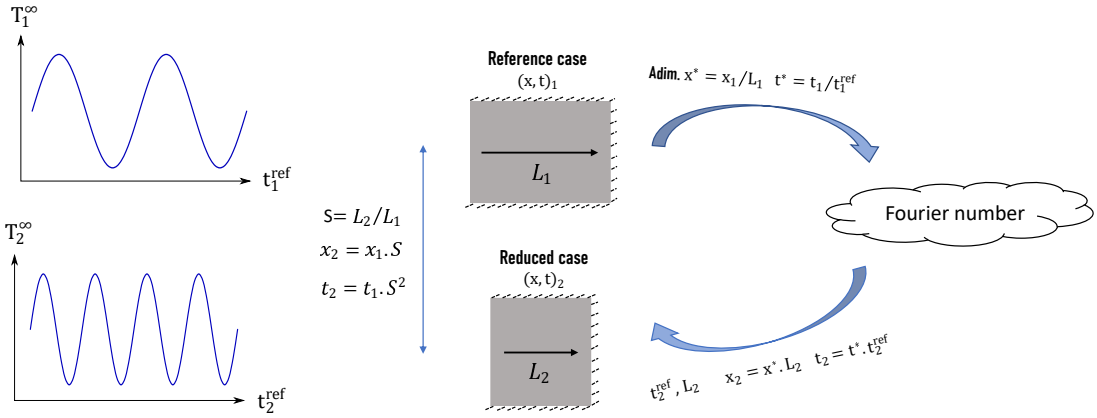

Figure 1. *The mapping of two equivalent configurations*

The Fourier number is the unique parameter in the dimensionless equation. By means of this characteristic number, a similarity can be established between the reference case where $x \in \Omega_x^1$, $t \in \Omega_t^1$ and the equivalent case such that $x \in \Omega_x^2$, $t \in \Omega_t^2$. With:

$$\Omega_x^i = \{\, x \in \mathbb{R}^+, 0 \leq x \leq L_i \,\} = [\,0\,,\, L_i\,]\,, \tag{14a}$$

$$\Omega_t^i = \{\, t \in \mathbb{R}^+, 0 \leq t \leq t_i^{ref} \,\} = [\,0\,,\, t_i^{ref}\,]\,, \qquad \forall i \in \{\,1\,,\,2\,\}\,. \tag{14b}$$

where i refers to the number of the experiment configuration. Two different configurations 1 and 2 are said to be equivalent or similar if they verify the following equality :

$$\mathrm{Fo}_q^1 = \mathrm{Fo}_q^2\,. \tag{15}$$

As a reminder, both experiments have been carried out on two samples, made of the same material. Moreover, we assume that these samples have the same porosity and initially the same hydric state. This means : $k_{q1}^{\mathrm{ref}} = k_{q2}^{\mathrm{ref}}$, $c_{q1}^{\mathrm{ref}} = c_{q2}^{\mathrm{ref}}$ and $\rho_1^{\mathrm{ref}} = \rho_2^{\mathrm{ref}}$. Thus, Eq. (15) is simplified to :

$$\frac{t_2^{\mathrm{ref}}}{t_1^{\mathrm{ref}}} = \left(\frac{L_2}{L_1}\right)^2. \tag{16}$$

We defined the proportionality factor between the two configurations by:

$$\Sigma = \frac{L_2}{L_1}\,. \tag{17}$$

Σ designates the ratio between two characteristic lengths L_1 and L_2. These represent the dimensions according to which, the heat transfer occurs in both configurations. Mathematically, we carry out a mapping, based on the dimensionless numbers, from a first configuration to a second by applying the proportionality factor Σ.

$$\Omega_x^1 \times \Omega_t^1 \longrightarrow \Omega_x^2 \times \Omega_t^2 \tag{18a}$$

$$(\,x_1\,,\,t_1\,) \longmapsto (\,x_2 = x_1 \cdot \Sigma\,,\, t_2 = t_1 \cdot \Sigma^2\,) \tag{18b}$$

The next section will define the adopted experimental protocol. First, we define the material studied and its manufacturing phase. This is followed by a description of the equipment and the sensors used. Finally, the experimental configurations are highlighted, allowing us to verify the validity of the hypotheses.

3 Materials and experimental facility

We chose hemp concrete for the similar tests. It is a bio-based composite material made of hemp and lime (Fig. 2). The material was manufactured using the following products: Biofibat, a calibrated hemp aggregate with a density of $\rho = 110\,[\mathsf{kg.m^{-3}}]$ and $k_q = 0.05\,[\mathsf{W.m^{-1}.K^{-1}}]$ and a moisture content of less than 15%, and Tradical$^{\mathrm{R}}$ PF 70, a class FL A 3.5 formulated lime in accordance with the NF EN 459 standard where $\rho = 620\,[\mathsf{kg.m^{-3}}]$ and $k_q = 0.096\,[\mathsf{W.m^{-1}.K^{-1}}]$.
The hemp concrete formulation was based on the proportions, defined by the French standard, which are 16% hemp, 34% lime and 50% water. Moreover, the homogenization of the mixture was ensured using a mixer for approximately three minutes. We let the mixture cure for 10 days in molds of $15 \times 15 \times 15\,\mathsf{cm^3}$. The molds were also treated with an agent to facilitate the release of samples. The experimental characterization of hemp concrete thermal properties under this formulation [3], provides the following results $k_q = 100.23\,[\mathsf{mW.m^{-1}.K^{-1}}]$, $c_q = 5.52\,10^5\,[\mathsf{J.m^{-3}.K^{-1}}]$ and $\rho = 480\,[\mathsf{kg.m^{-3}}]$.

Figure 2. *Lime and hemp used in the process*

In addition, we used a climatic chamber brand Climats (Fig. 5(a)) which can generate stress scenarios such as a variation in temperature and relative humidity. We mainly used it to simulate thermal stress in our study, with a humidity set at 85%. An Almemo (Ahlborn) acquisition unit and series FHA 646 R Ahlborn sensors were used. The Ahlborn FHA 646 R is a cylindrical sensor with a $5\,\mathsf{mm}$ diameter, and can be used within a range from -30 to $100\,^{\circ}\mathsf{C}$ and from 5 to 95% relative humidity. These sensors are calibrated at $23\,^{\circ}\mathsf{C}$, 35% and 80% relative humidity. The factory calibration certificate indicates an accuracy of $0.3\,\mathsf{K}$ in temperature and $\pm 3\%$ in relative humidity. The response time of the sensor is around $10\,\mathsf{s}$ estimated at $1\,\mathsf{m/s}$ air velocity. The samples manufactured and the equipment described were used for the three tests. Two tests verify the limitations of Hypotheses 1 and 3 and the third is devoted to the validation of thermal similarity.

3.1 The one-dimensional transfer

The sample is a $10 \times 10 \times 10\,\mathsf{cm^3}$ cube, initially preconditioned at $85\,\%$ relative humidity and $25\,^{\circ}\mathsf{C}$ in the climatic chamber, as shown in Fig. 5(a). The material was isolated from four sides using a $3\,\mathsf{cm}$ layer of industrial polystyrene with a thermal conductivity of $k_q = 0.035\,[\mathsf{W.m^{-1}.K^{-1}}]$, to limit the flux perpendicular to the chosen direction of transfer. In fact, the measured thermal conductivity of hemp concrete is almost

three times higher than that of the insulation used. Hemp concrete is still three times less efficient than the current insulators used, namely rock or glass wool where $k_q \in [0.03, 0.04]\,[\mathsf{mW.m^{-1}.K^{-1}}]$. In order to maintain a good bond between the concrete and the insulation, we attached two layers of an aluminum adhesive ribbon to the assembly (Fig. 5(b)).

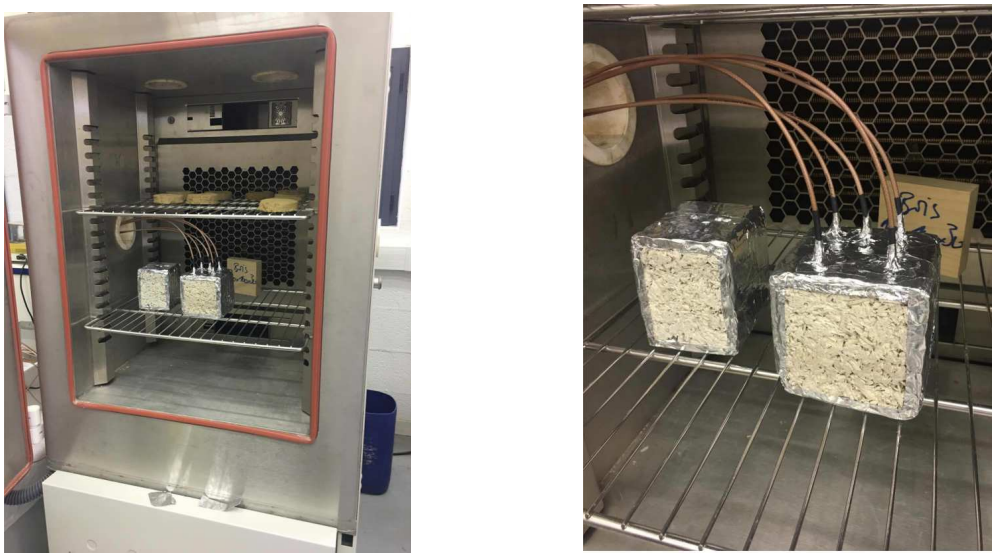

(a) (b)

Figure 3. *The climatic chamber (a) and the tested sample (b).*

Table 1. *Sensor position coordinates*

	x [cm]	y [cm]
χ_1	2.5	2.5
χ_2	2.5	5
χ_3	2.5	7.5
χ_4	7.5	2.5
χ_5	7.5	7.5

Six sensors were used with a diameter of 5 mm and a height of 5 to 7 cm, we positioned five within the sample at a height of 5 cm, the corresponding coordinates were given in Table 1. The sensors formed two rows, the first at a depth of 2.5 cm (three sensors) and the second at 7.5 cm (two sensors) as shown in Fig. 4. We used the last one to read the value of T and ϕ of the ambient air. We consider making an error during the positioning of sensors. The error is of the same magnitude as the sensor diameter and will be useful for the calculation of uncertainties. This first experiment aims to evaluate the thermal flux along the y-axis. The hypothesis is validated as long as this flux is negligible.

3.2 The Dirichlet approximation

The same sample used for **Hypothesis 1** was adopted for the next test. Fig. 5 represents the experimental protocol to verify the assumption made about the Dirichlet boundary condition. The configuration was exactly the same, with four sensors this time. The first two measured air temperature and the last ones were fixed on the surface of the material and measured its temperature. The sensors on the surface were not isolated, based on the assumption that there were no radiation effects in the chamber. They were embedded within the sample surface and fixed using an adhesive ribbon. This enabled an almost perfect

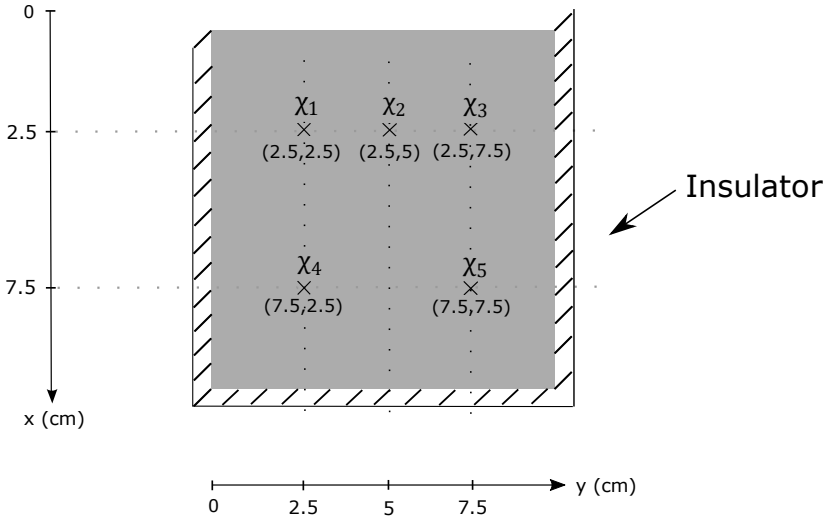

Figure 4. *Sensor positions in the sample*

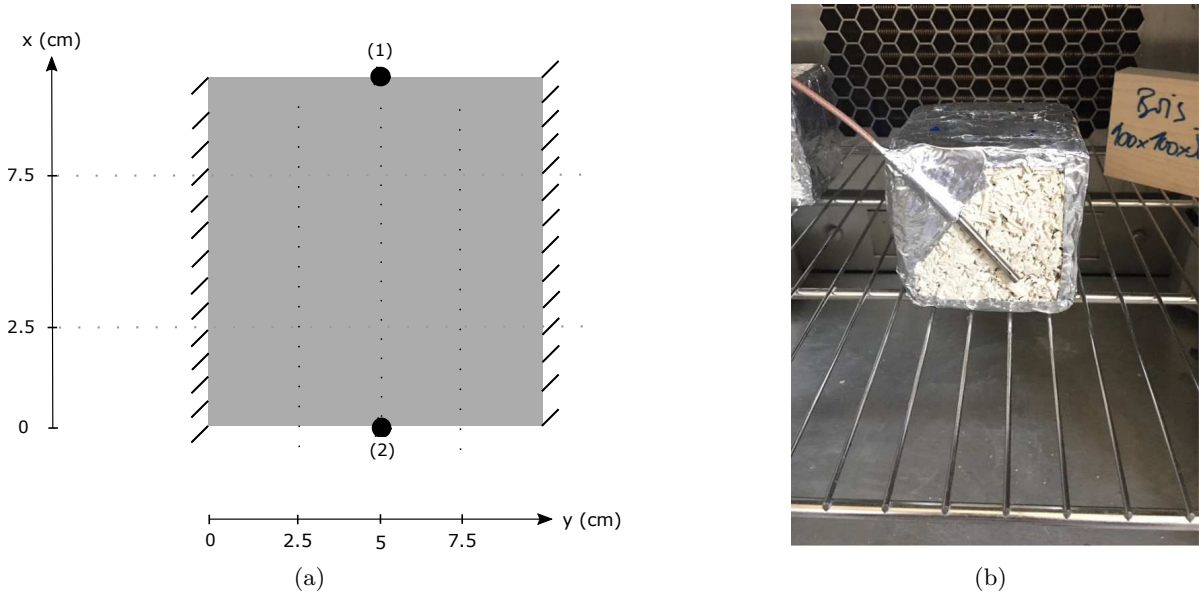

Figure 5. *The climatic chamber (a) and the tested sample (b).*

sensor-surface adherence. The integrated fan in the climate chamber operated at a constant and nominal flow rate. The material was placed inside the chamber in such a way as to allow the surface $x = 10\,\mathsf{cm}$ to be perpendicular to the ventilation direction. The purpose of this second test was to measure the temperature variation at the surfaces $x = 0\,\mathsf{cm}$ and $x = 10\,\mathsf{cm}$. It was then compared to the ambient air temperature.

3.3 Experimental thermal similarities

Previously, we explained the procedure for the verification and validation of the predefined hypotheses. This step is necessary in order to control relatively the conditions of both configurations obtained via the similarity laws. This section consists in the presentation of the two tests that aim to verify these laws experimentally. Both test samples were from the same formulation of hemp concrete. After the curing period, both samples were stored at 25 °C and 85% relative humidity. Therefore, we consider a reference configuration where samples are cubic and have the size of the molds. Using the laws of similarity, we want to reduce the duration of the test that represents the reference configuration. A reduction calls for

the application of a proportionality factor lower than 1, we chose $0 < \Sigma < 1$. Thus, a sample having a thickness L_1 was taken, then a second one was selected, and sliced to reduce its thickness to L_2 such that $L_2 = \Sigma\, L_1$ (Fig. 6). Next, the materials were similarly preconditioned in temperature and relative humidity. Subsequently, they underwent a thermal stress according to two well-defined scenarios. These scenarios must have the same amplitudes and verify the following equality: $t_2^{\text{ref}} = \Sigma^2\, t_1^{\text{ref}}$.

Figure 6. *Samples for the similarity experiment*

4 Uncertainty propagation in the measurements

Experimental measurements are sensitive to errors of various kinds. Some of them may be due to the experimenter's lack of expertise. They can also be affected by the systematic accuracy of an equipment. It is therefore necessary to include the confidence interval in a study. In this regard, we introduce the notion of uncertainties [43]. For similarity tests, we define the total uncertainty as:

$$\sigma_{Tot}^2 = \sigma_x^2 + \sigma_t^2 + \sigma_\phi^2 + \sigma_{\mathsf{Sys}}^2 + \sigma_{\mathsf{Rdm}}^2 + \sigma_{\mathsf{Dlt}}^2 + \sigma_{\mathsf{1D}}^2 + \sigma_{\mathsf{Sensor}}^2 \,. \tag{19}$$

The assessment of the global uncertainty σ_{Tot} is based on the evaluation of the different contributions. They are explained starting with σ_x, which is the uncertainty associated with the sensor location regarding the desired measurement position:

$$\sigma_x(\,t\,) = \frac{\partial T}{\partial x}\,\delta_x \,. \tag{20}$$

The temperature derivative is thus evaluated at the same position. This is possible by computing the model in Eq. (4) using the implicit Euler method and central finite-differences. δ_x represents the average error made and estimated by the experimenter when positioning the sensor. σ_x is a time function because temperature and its derivative are.

The reaction time of a sensor can also be a source of uncertainty. A sensor that requires 1 minute to measure a change in temperature is less accurate than one that takes only 10 seconds to respond. σ_t is the uncertainty regarding the response time. It displays the time derivative of temperature.

$$\sigma_t(\,t\,) = \frac{\partial T}{\partial t}\,\delta_t \,. \tag{21}$$

This derivative is evaluated at the measurement position and throughout the test. It was calculated using the same model as for σ_x. The response time is given by the term δ_t.

After introducing the vapor pressure and temperature model, we simplified both equations, considering the small impact of relative humidity on temperature. This implies the omission of the term $\nabla\, P_v$ in heat and

mass transfer equations [44, 45]. In order to estimate the uncertainty due to the decoupling of temperature and vapor pressure, we evaluate the parameter σ_ϕ.

$$\sigma_\phi(t) = \frac{\partial T}{\partial \phi}\,\delta_\phi = \frac{\partial T}{\partial t}\left(\frac{\partial \phi}{\partial t}\right)^{-1}\delta_\phi\,. \tag{22}$$

Its estimation would be based on the solution of coupled heat and mass transfer equations [46–48]. The initial condition is the one reached by the material after the preconditioning phase. Moreover, the boundary conditions used are the measured temperature and relative humidity at the surface of the material throughout the experiment. The term δ_ϕ is the difference between the relative humidity at an instant t and the one at the initial state of the sensor position.

The sensor as a conceived system is an uncertain device in terms of measurement, and represents a systematic uncertainty. Indeed, the manufacturer performs calibration tests on the sensor to define its margin of error. Thus, this uncertainty is indicated within the product record. It is constant and requires no calculation, we denote it σ_{Sys}.

The random experimental uncertainty is also proposed and defined. It is obtained by the principle of repeatability. A sample undergoing the same experiment several times, can lead to different results. In this case, the values obtained approximate a mean value which is the one generally retained by the experimenter. Let N be the number of tests carried out, T the measured temperature and $\bar{T}$ the average value of the measurements, the random uncertainty σ_{Rdm} is estimated as follows:

$$\sigma_{\mathsf{rdm}} = \frac{1}{\sqrt{N}}\sqrt{\frac{1}{N-1}\sum_{i=1}^{N}(T_i-\bar{T})^2}\,, \qquad \bar{T} = \frac{1}{N}\sum_{i=1}^{N}T_i\,. \tag{23}$$

Furthermore, we estimate the errors resulting from the Dirichlet approximation discussed in Section 3.2. This is performed through a sensitivity analysis regarding the surface temperature. The uncertainty related to this hypothesis is determined by the following expression :

$$\sigma_{\mathsf{Dlt}}(t) = \frac{\partial T}{\partial T_s}\,\delta_{T_s}\,. \tag{24}$$

where T_s is the temperature at the surface of the material and δ_{T_s} is the difference between both air and surface temperatures at an instant t, discussed previously in Eq. (44). The temperature derivative can be calculated numerically. For this, we performed a differentiation of Eq. (4) according to the variable T_s:

$$\frac{\partial}{\partial T_s}\left(\rho\, c_q \frac{\partial T}{\partial t}\right) = \frac{\partial}{\partial T_s}\left(\frac{\partial}{\partial x}\left(k_q \frac{\partial T}{\partial x}\right)\right). \tag{25}$$

Since the temperature is twice derivable and its derivatives are continuous, we can invert the order of the derivation (Schwartz theorem). The thermal properties are assumed constant. A new variable θ is introduced and defined by $\theta = \dfrac{\partial T}{\partial T_s}$, so θ verifies the following equation:

$$\rho\, c_q \frac{\partial \theta}{\partial t} = \frac{\partial}{\partial x}\left(k_q \frac{\partial \theta}{\partial x}\right). \tag{26}$$

The equations expressing the boundary conditions of our problem are also derived according to the surface temperature and become:

$$\theta = 1\,, \quad x = 0\,,\, t \in \Omega_t\,, \qquad \frac{\partial \theta}{\partial x} = 0\,, \quad x = L\,,\, t \in \Omega_t\,. \tag{27}$$

Finally, at the initial state we obtain:

$$\theta = 0 \quad at \quad t = 0\,. \tag{28}$$

Equations (26), (27) and (28) constitute a closed mathematical system that we solve numerically via the implicit Euler method as well. Thus, the variable $\theta\,[-]$ is evaluated at all test instants and that enables to compute σ_{Dlt}.

On the other hand, the uncertainty related to **Hypothesis 1** σ_{1D} (one-dimensional transfer) is estimated by means of the test carried out to validate it. Theoretically, the exact evaluation of σ_{1D} is given by the following formula [43]:

$$\sigma_{\,\mathsf{1D}} = \lim_{N\to+\infty} \Big(\frac{1}{N\,(\,N-1\,)} \sum_{i=1}^{N} (\,T_i - \bar{T}\,)^{\,2} \Big)^{\,0.5} . \tag{29}$$

where :

$$\bar{T} = \lim_{N\to+\infty} \frac{1}{N} \sum_{i=1}^{N} T_i\,. \tag{30}$$

N represents the number of sensors placed inside the material along the y-axis while fixing the x coordinate

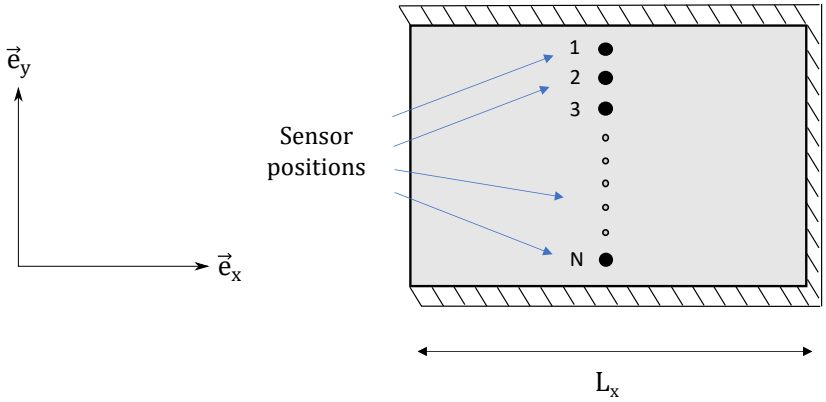

Figure 7. *Sensor positions for the evaluation of the one dimensional transfer hypothesis*

(Fig. 7). According to Eq. (29), the uncertainty is exact if the positions number is infinite. However, given experimental constraints, it is quite difficult to achieve this condition. Indeed, the material dimension along the y-axis, which is $y_{max} = 10\,\mathsf{cm}$, does not allow the placement of more than five sensors having a $5\,\mathsf{mm}$ diameter. Furthermore, we restricted ourselves to three to avoid interactions between sensors and perturbation of heat transfer. We used temperature measurements at the three positions χ_1, χ_2 and χ_3 (Fig. 4). Furthermore, the formula in (29) is adopted, which is normally used for the evaluation of random uncertainty, and applied to these three positions according to Eq. (32). $\bar{T}$ designates the arithmetic mean of the three measured temperatures.

$$\bar{T} = \frac{1}{3} \sum_{i=1}^{N=3} T_i\,. \tag{31}$$

$$\sigma_{\mathsf{1D}} = \frac{1}{\sqrt{3}} \sqrt{\frac{1}{2} \sum_{i=1}^{N=3} (\,T_i - \bar{T}\,)^2}\,. \tag{32}$$

Then, the last sub-uncertainty denoted σ_{Sensor}, is defined and introduced it in Eq. (19). σ_{Sensor} considers the error related to the sensor rate of adherence on the sample surface. The sensor set-up shown in Fig. 5, measures an area weighted mean temperature as opposite to the surface area. This is due to the fact that the sensor is not protected against the surrounding air, it adheres to the surface on the one hand and is exposed to air on the other. Uncertainty σ_{Sensor} is defined according to the following expression:

$$\sigma_{\mathsf{Sensor}}\,(\,t\,) = \frac{\partial T}{\partial T_{\mathsf{Sensor}}}\,\delta_{\,\mathsf{Sensor}}\,. \tag{33}$$

Equation (33) contains two time-dependent terms. The first represents the temperature partial derivative according to the mean temperature T_{Sensor} which is that recorded by the surface sensor. This derivative is assessed in the same way as in Eq. (24). The sensitivity analysis remains the same in this instance, while considering that the surface temperature is not that given by the sensor. The second term is the error between the true surface temperature T_s and that measured by the sensor T_{Sensor}. It is denoted $\delta_{\mathsf{Sensor}}\,[\mathsf{°C}]$ and its expression is given below :

$$\delta_{\mathsf{Sensor}}(t) = \left| T_{\mathsf{Sensor}} - T_s \right|. \tag{34}$$

The goal is to evaluate the error δ_{Sensor}, and for this purpose we express the temperature measured by the sensor as the weighted mean of air and the real surface temperature denoted T^∞ and T_s respectively. Mathematically, the sensor temperature is given in Eq. (35) :

$$T_{\mathsf{Sensor}}(t) = \frac{T_s S_s + T^\infty S^\infty}{S_{Tot}}. \tag{35}$$

Where S_s, S^∞ and $S_{Tot}\,[\mathsf{m}^2]$ represent sensor surfaces in adherence to the sample surface, exposed to the ambient air and the entire surface of the sensor (Fig. 8). These terms verify the following equality :

$$S_{Tot} = S_s + S^\infty \tag{36}$$

Thus, we deduce the sample surface temperature:

$$T_s = \frac{S_{Tot}}{S_s}\left(T_{\mathsf{Sensor}} - \frac{S^\infty}{S_{Tot}} T^\infty\right). \tag{37}$$

T_{Sensor} and T^∞ are determined experimentally using the two sensors shown in Fig. 5. In addition, the area

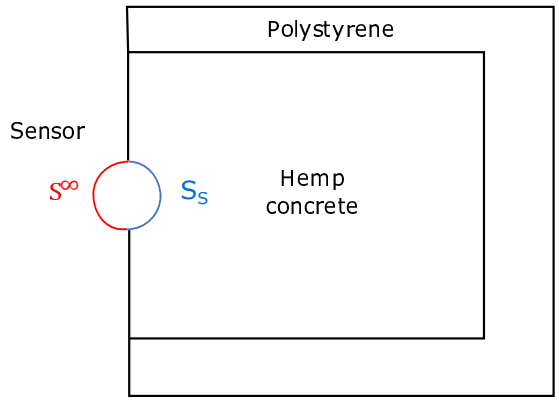

Figure 8. *The set-up adopted for the temperature sensor on the sample surface. The sensor has been increased for the illustration.*

terms in Eq. (35) are set respecting the conditions of the Hypothesis 2 experiment. Finally, this information enables us to deduce the error time variation δ_{Sensor} and thus the uncertainty σ_{Sensor} at the desired position χ.

5 Results and discussion

5.1 Validation of the one-dimensional transfer (Hypothesis 1)

After the preconditioning phase, the sample was exposed to a temperature sinusoidal stress, with an amplitude of 14°C and a mean value of 25°C, where the period $\Gamma = 24\,\mathsf{h}$. The relative humidity was maintained at ϕ_0 (Fig. 9). The aim is to determine the quantities or expressions in order to assess the

Hypothesis 1. We consider the heat transfer coefficient constant. Thus, in order to obtain a similar expression to that in Eq. (4), we need to ensure that :

$$\frac{\partial^2 T}{\partial y^2} \leqslant \epsilon\,, \quad \forall t \in \Omega_t\,. \tag{38}$$

where y is the second space coordinate and ϵ represents a constant close to zero. This derivative can be approximated by a centered numerical scheme of second order. The approximation, at $x = x_2$, is given by the following relation, where $\Delta y = y(\chi_2) - y(\chi_1)$:

$$\frac{\partial^2 T}{\partial y^2} \simeq \frac{T(\chi_1) - 2\,T(\chi_2) + T(\chi_3)}{\Delta y^2} + o(\Delta y^2). \tag{39}$$

Therefore, during an experimental test, the measurements recorded on the nodes 1, 2 and 3 are used to verify the following equality:

$$T(\chi_1) - 2\,T(\chi_2) + T(\chi_3) = 0\,. \tag{40}$$

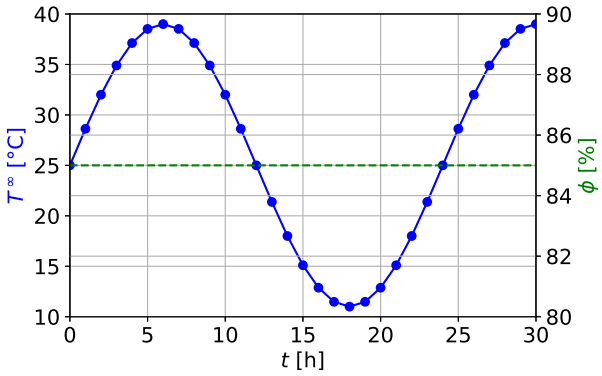

Figure 9. *boundary conditions set by the climatic chamber*

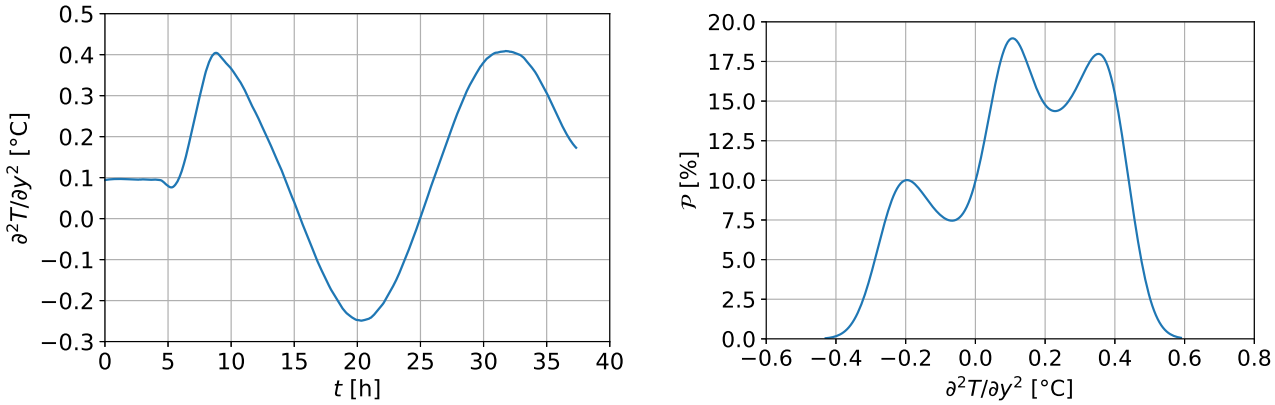

(a) (b)

Figure 10. *Temperature second derivative (a) and its value distribution (b)*

By means of the quantity introduced in Eq. (40), it is possible to evaluate the order of magnitude of the second temperature derivative along the y axis, at each instant. Figs. 10(a) and 10(b) illustrate the variation of this quantity, as well as the distribution of its values. This distribution is evaluated using the calculation of the probability density $\mathcal{P}$ associated with the temperature second derivative along y. The

probability density $\mathcal{P}$ is a function of a continuous random variable, whose integral across an interval gives the probability that the value of the variable lies within the same interval. In this work, we adopt the Kernel distribution as a probability density function. The quantity evaluated is about 0.1 °C during the preconditioning phase. During the stress period, it varies in a sinusoidal shape between 0.1 and 0.4 °C (Fig. 10(a)). Figure 10(b) shows that propagation of the values is almost uniform. Indeed, the probability density varies from 10 to 20% over a large range of values. Thus, it is deduced that the hypothesis can be confirmed with a maximum error of $\epsilon = 0.4$ °C.

It is also possible to argue in terms of flow. The direction x is favored in transfer over the others if $\frac{\partial T}{\partial x} \gg \frac{\partial T}{\partial y}$ and $\frac{\partial T}{\partial x} \gg \frac{\partial T}{\partial z}$. With the sensors we dispose of, it is possible for example to compare the thermal flux φ_x and φ_y along the x and y axis respectively. Using a first order upward scheme at node 4, we can write :

$$\varphi_y = \left| -k_q \frac{\partial T}{\partial y} \right| \simeq \left| -k_q \frac{T_5 - T_4}{y_5 - y_4} \right|, \qquad \varphi_x = \left| -k_q \frac{\partial T}{\partial x} \right| \simeq \left| -k_q \frac{T_1 - T_4}{x_1 - x_4} \right|. \tag{41}$$

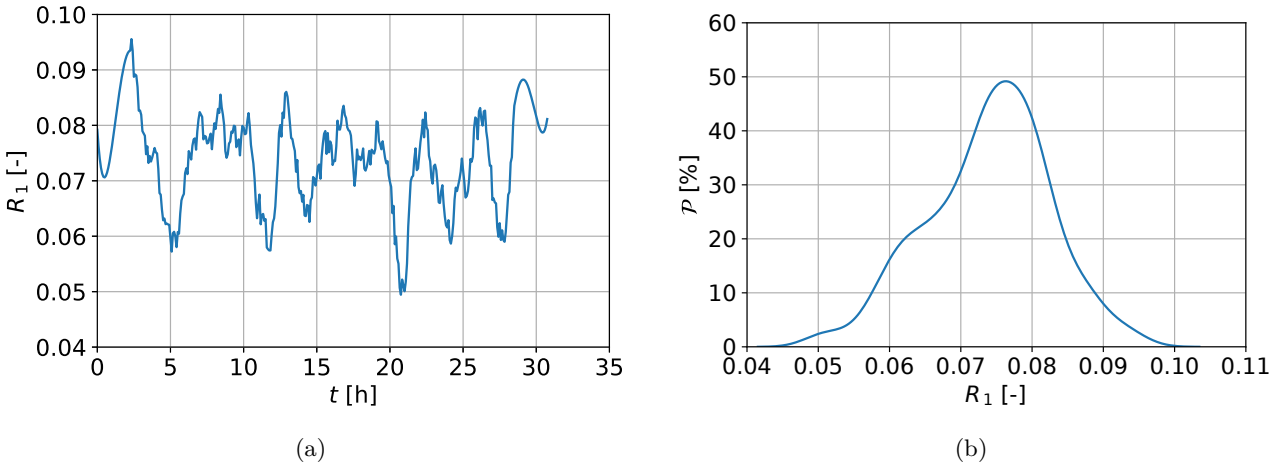

(a) (b)

Figure 11. *The heat flow along the y axis related to the one along the x axis (a) and the ratio values distribution (b).*

given that $\Delta x = x_1 - x_4 = y_5 - y_4 = \Delta y$. We can define the ratio R_1, which represents the quotient of the two introduced fluxes. R_1 is calculated as follows:

$$R_1 = \frac{\varphi_y}{\varphi_x}. \tag{42}$$

R_1 compares the order of magnitude of the studied fluxes. It is evaluated during the same experiment, and its variation is shown in Fig. 11(a). The values can be as low as 0.05 and up to 0.09. This means that the flux along the y axis is 10 to 20 times smaller than the one along x. This is mainly due to the fact that the x-axis direction is privileged when insulating the surrounding faces. This aspect can be reinforced by increasing the length and increasing the thermal insulation. Fig. 11(b) shows the distribution of the ratio values. It is around 0.075 for a probability of 50%. In addition, a complementary investigation was developed to evaluate the error due to the one-dimensional transfer design. A comparative numerical study was performed between the proposed one-dimensional case and the experimental case. On the one hand, the experimental case reproduces the realistic conditions in the climate chamber as shown on the left in Fig. 12(a).

Figure 12(b) represents the lumped approach modeled in one-dimension as considered in our work. In this case, a 4 cm polystyrene thickness and a convective coefficient $h_c = 5\,[\mathrm{W.m^{-2}.K^{-1}}]$ are considered. On

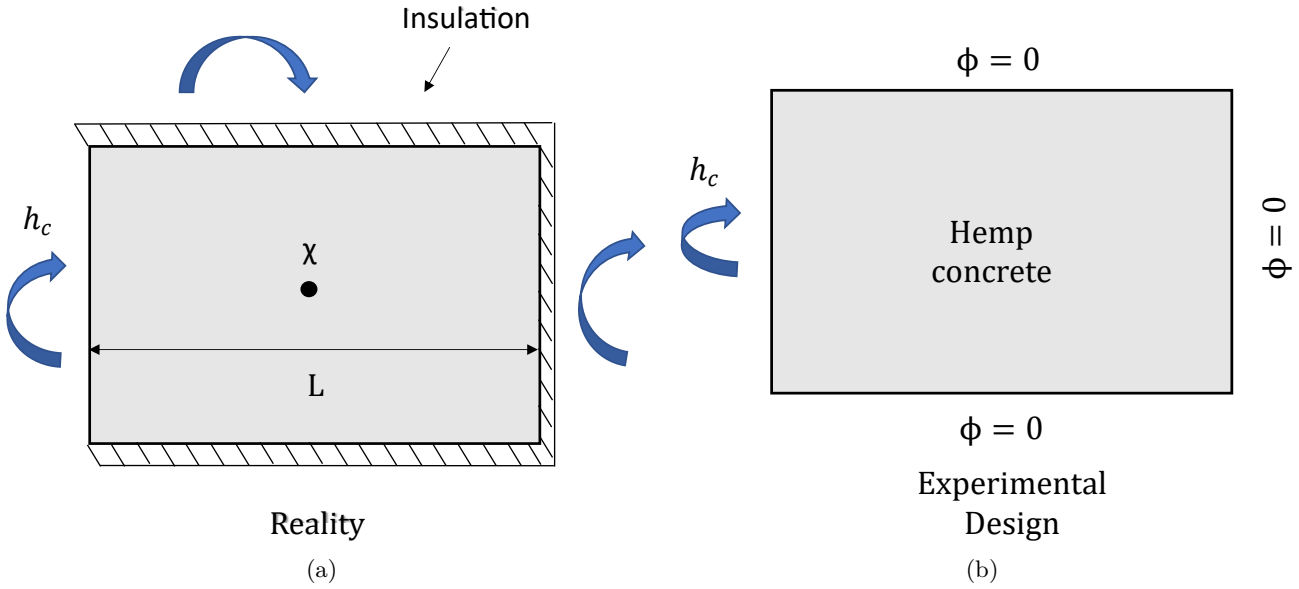

Figure 12. *(a) Realistic model of the experiment in two dimensions, (b) lumped approach in one dimension*

the other hand, the ideal case consists of considering perfectly adiabatic walls where the heat flux equals 0; see Fig. 12(b). Numerical computations of the temperature for both cases were carried out using COMSOL software. Indeed, the method used in the experimental design (Eq. (41)) is an approximation employing the following meshes $\Delta x = \Delta y = 5\,\mathsf{cm}$. Thus, to overcome this issue we performed a numerical simulation using smaller meshes $\Delta x = \Delta y = 10^{-3}\,\mathsf{cm}$. Both materials were modeled considering $4\,\mathsf{cm}$ and $10\,\mathsf{cm}$ thickness for polystyrene and hemp concrete respectively. The Robin type was considered for boundary conditions where $h_c = 17\,\mathsf{W.m^{-2}.K^{-1}}$ as a conventional value and T^∞ was provided by the ambient air sensor.

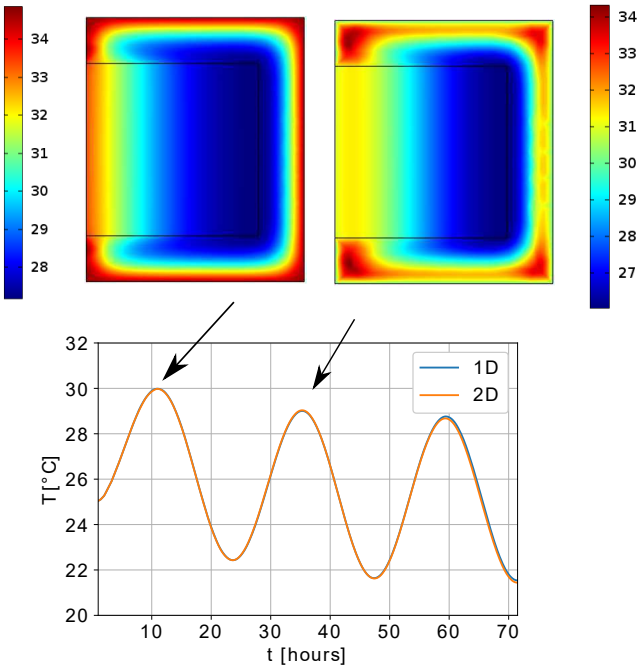

Figure 13. *Temporal temperature evolution at the middle of the sample between the 1D and 2D heat transfer approach*

Fig. 13 presents the variation of temperature at the middle of the sample for both approaches. As

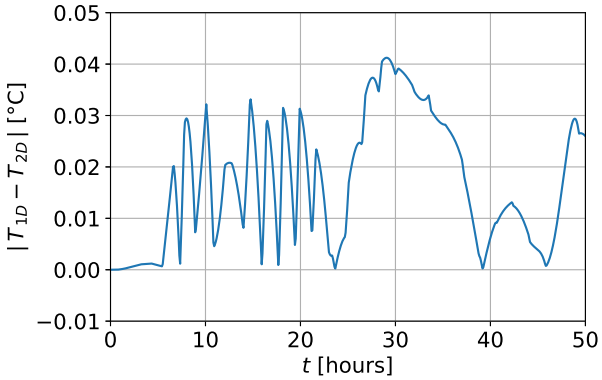

Figure 14. *Temperature error evaluation at the middle of the sample between the two approaches.*

shown in Fig. 13, the temperature variation when adopting the experimental design is close to that of the theoretical 1D model. In addition, errors are noticeable, for example at the instants $t = 10, 35, 58\,\mathsf{h}$. The overall error variation at the middle of the sample is given in Fig. 14. The error is small and ranges from 0 to $0.04\,^{\circ}\mathsf{C}$. A second investigation consisted in the numerical evaluation of R_1 at the same position used for measurements. Its time variation, using a logarithmic scale, is illustrated in Fig. 15. Notice that R_1 is

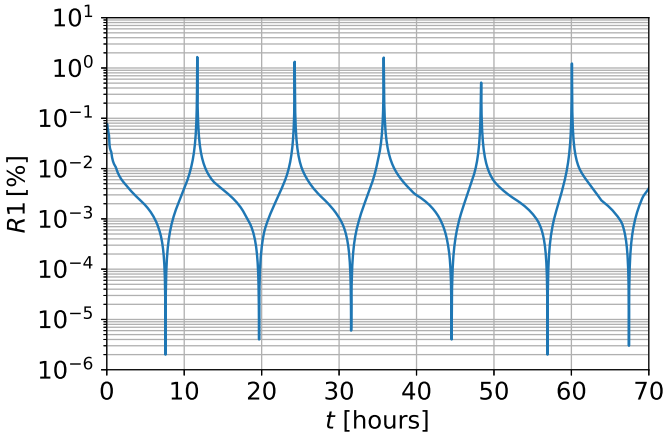

Figure 15. *Variation of the heat flux ratio* R_1

smaller than the one assessed experimentally. It is almost zero during long time sequences. In addition, there are some instants where the ratio reaches maximum values of about 1.1 %. The choice of a mesh size equal to $10^{-3}\,\mathsf{cm}$ along the x and y axis was sufficient to obtain a numerical solution with a suitable accuracy. This was deduced by performing a study of sensitivity according to the mesh size. In this framework, two additional simulations, where $\Delta x = \Delta y = 10^{-5}\,\mathsf{cm}$ and $\Delta x = \Delta y = 10^{-7}\,\mathsf{cm}$, were performed while maintaining the same time step. The study revealed that the variation of the ratio R_1 is almost the same for smaller mesh sizes. In terms of deviation, a maximum value of 10^{-8} was reached when comparing the three variations. Thus, choosing smaller mesh sizes did not have a significant influence on the magnitude of this numerical result. Another study was performed to analyze the heat map of our configuration following two instants. Both heat maps are illustrated in Fig. 13. It is worth noting that the isothermal lines obtained are perpendicular to the direction along x in hemp concrete. If we focus on the insulation material, the isothermal lines have no longer this characteristic. This means that heat transfer in hemp concrete tends to be one-dimensional. Moreover, it is possible to confirm this by studying flux streamlines. Fig. 16 plots these at the same instants. Notice that heat flux is mostly along the x direction in the studied material.

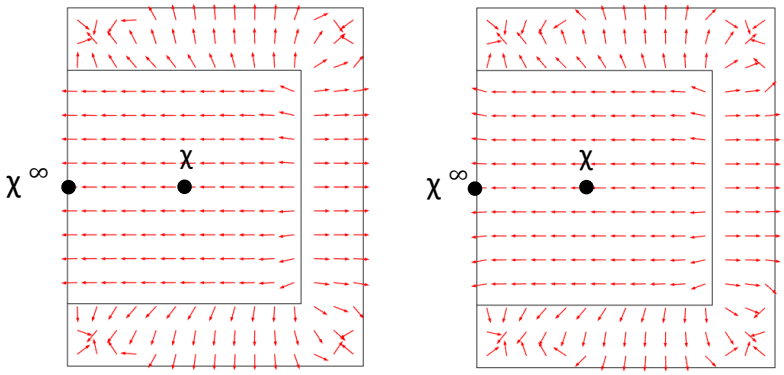

Figure 16. *Streamlines representing the heat flow direction within the hemp concrete and the insulator at two different instants (a) $t = 10\,h$ and (b) $t = 35\,h$*

5.2 Validation of the Dirichlet approximation (Hypothesis 2)

In a realistic case, the boundary condition of a material in contact with a fluid is defined as follows:

$$-\frac{\partial T}{\partial x} = \frac{h_c}{k_q}\left(T^{\infty} - T\right), \qquad x = 0\,. \tag{43}$$

This is the Robin boundary condition, where $T^{\infty}\,[\mathsf{K}]$ is the ambient temperature and $h_c\,[\mathsf{W/(m^2.K)}]$ the surface heat transfer coefficient. Notice that, if h_c is large or the thermal conductivity is small, we face a situation where thermal flux is large. Thus, the equality (43) is possible as long as we verify that $T \simeq T^{\infty}$ at the material surface, which corresponds to the Dirichlet condition.

The two considered hypotheses for the convective thermal coefficient and thermal conductivity can be approached experimentally. A material with high insulating potential can be chosen. Moreover, the coefficient depends on the nature of the fluid flow and the surface imposed to the impact. In particular, it depends on the flow velocity according to the Nusselt number. Hemp concrete has a good insulating potential which is characteristic of hemp concrete. In addition, we studied the condition regarding the thermal coefficient h_c. Based on the position of the sensors in the configuration (Fig. 5), the goal is to verify the following expression:

$$\left|\,T\,(x=0,t) - T^{\infty}\,\right| \leqslant \epsilon\,, \quad \forall t \in \Omega_t\,. \tag{44}$$

A preconditioning phase not being necessary, we used the same stress adopted for the validation of the first hypothesis and shown in Fig. 9. The variation of both temperatures is shown in Fig. 17. We observe that the variation is almost the same as shown in Figs. 18(a) and 18(b). Indeed, the comparison over two different time ranges highlights the quasi-superposition of both curves.

In addition, it was possible to evaluate the discrepancy throughout the experiment as well as its corresponding distribution (probability density). It ranges from 0.075 to 0.225 °C (Fig. 19(a)). It was also demonstrated that it is centered around 0.15 °C as shown in Fig. 19(b). Under similar conditions and with regard to these results, Hypothesis 2 is validated, with an uncertainty on surface temperature reaching 0.225 °C. Thus, $\delta_{T_s} = 0.225$ °C.

5.3 Assessment of thermal similarity

5.3.1 Definition of the case

Calculation of the uncertainties is necessary in combination with the results of experimental work. It helps defining the acceptable margin of uncertainty on a measured quantity. After having introduced the seven sub-uncertainties, they are evaluated for both configurations. The reference configuration is given

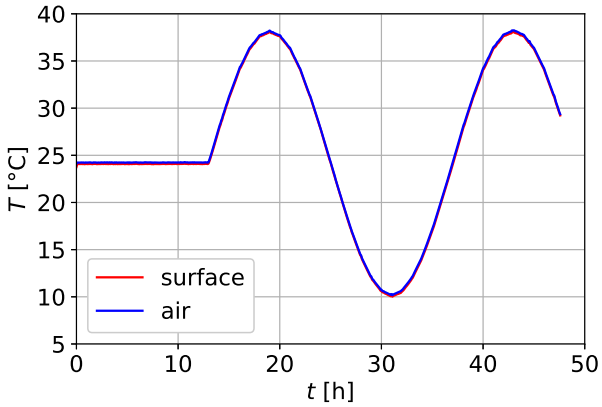

Figure 17. *Variation of air and material surface temperatures during the preconditioning and the stress phases*

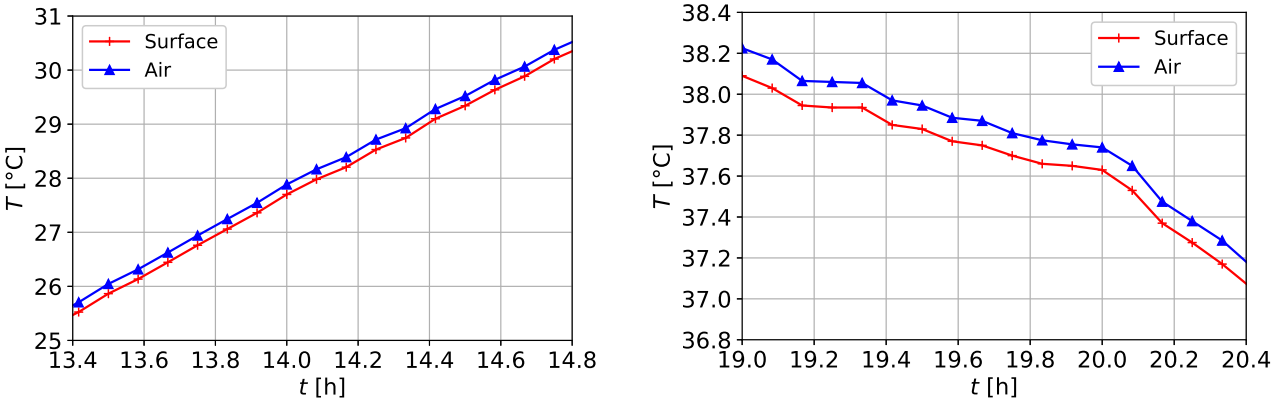

(a) (b)

Figure 18. *Air and material surface temperatures at two different experiment sequences*

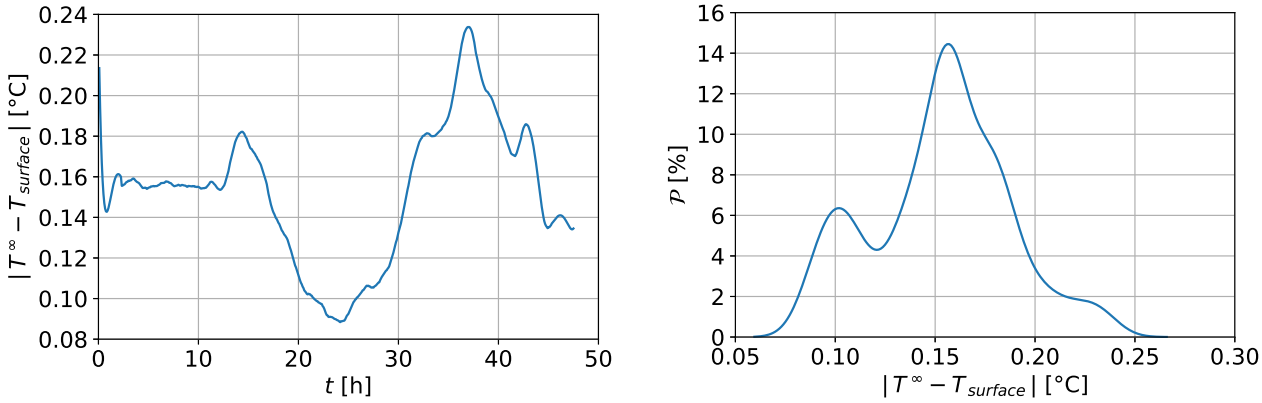

(a) (b)

Figure 19. *The calculated discrepancy between the measured air and material surface temperatures (a) discrepancy distribution throughout the experiment*

using a $L_1 = 15\,\mathsf{cm}$ thick material. This sample is exposed to the same stress, that is presented in Fig. 9, where the experiment horizon is $t_1^{\mathrm{ref}} = 72\,\mathsf{h}$ and the time period $\Gamma_1 = 24\,\mathsf{h}$.

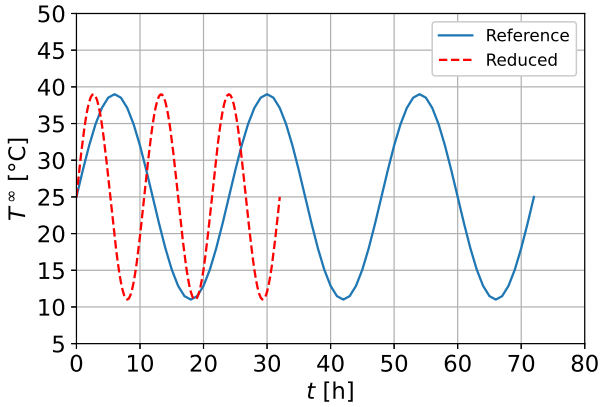

Figure 20. *The equivalent boundary conditions*

The equivalent configuration was based on a smaller sample with a thickness of $L_2 = 10\,\mathsf{cm}$. Thus, the factor of proportionality is $\Sigma = \dfrac{2}{3}$. By means of the expression in Eq. (15), a reduced experiment duration was obtained where $t_2^{\mathrm{ref}} = 32\,\mathsf{h}$ and $\Gamma_2 = 10.66\,\mathsf{h}$. The evaluation of uncertainties was limited to the middle values of both samples $x_1 = 7.5\,\mathsf{cm}$ and its equivalent $x_2 = 5\,\mathsf{cm}$. The boundary conditions defining the two configurations are illustrated in Fig. 20.

5.3.2 Evaluation of measurement uncertainties

We recall that the systematic uncertainty is $0.3\,°\mathsf{C}$ according to the manufacturer documentation. Its thermal response time is about $\delta_t = 10\,\mathsf{s}$. The sensor position uncertainty is approximately the diameter of the sensor, corresponding to $\delta_x = 5\,\mathsf{mm}$. It is worth noting that the uncertainties σ_x, σ_t, σ_{Dlt}, σ_{Sensor} and σ_ϕ are determined numerically. The first four are computed by solving Eq. (4) and using the implicit Euler scheme. The space and time meshes are given for both configurations: $\Delta x_1 = 1.5\,10^{-2}\,[\mathsf{cm}]$, $\Delta t_1 = 8.3\,10^{-2}\,[\mathsf{h}]$, $\Delta x_2 = 10^{-2}\,[\mathsf{cm}]$ and $\Delta t_2 = 3.6\,10^{-2}\,[\mathsf{h}]$. Furthermore, σ_ϕ is calculated using a coupled heat and mass transfer model [44]. This model was computed with the finite element solver COMSOL Multiphysics. The hemp concrete properties are issued from [2]. The random uncertainty is calculated by running three times the experiment for each configuration, therefore $N = 3$. Whereas, σ_{1D} is evaluated based on the experimental results for the sample shown in Fig. 4. Its thickness corresponds to the one of the reduced configuration sample. Thus, the results during t_2 are adopted for the reduced configuration. In the reference case, we consider that the results in terms of σ_{1D} are equivalent. Finally, the experimental configuration to evaluate the $\mathsf{hypothesis\,2}$ (Fig. 8) corresponds to a surface $S_s = 0.1\,S_{Tot}$. This means that the surface of the sensor, adhering to the sample, represents 10 % of its total surface. The processing of experimental and numerical data, as well as the plotting of curves is done using the programming language PYTHON.

Figure 21 highlights the time propagation of uncertainties related to the reference case at the middle of the sample. In order to compare, note that σ_x and σ_ϕ are of a significant order of magnitude. They attain values ranging from 0.2 to $0.6\,°\mathsf{C}$. Whereas σ_{Dlt} varies in the shape of an exponential increasing from 0 to $0.2\,°\mathsf{C}$. In parallel, σ_{1D} varies in a quasi-sinusoidal shape and reaches peaks of about $0.1\,°\mathsf{C}$. These instants correspond to the attainment of maximum air temperatures. Conversely, this uncertainty is small (less than $0.01\,°\mathsf{C}$) during the air-cooling phase. On the other hand, the uncertainties related to the thermal response of the sensor and the random aspect of the test are negligible. Regarding σ_{Sensor}, the evolution is quite the same between both configurations. Furthermore, each curve is almost periodic due to temperature stress periodicity. The uncertainty is quite zero at the beginning of the experiments and reaches a maximum value

of 0.18 °C.

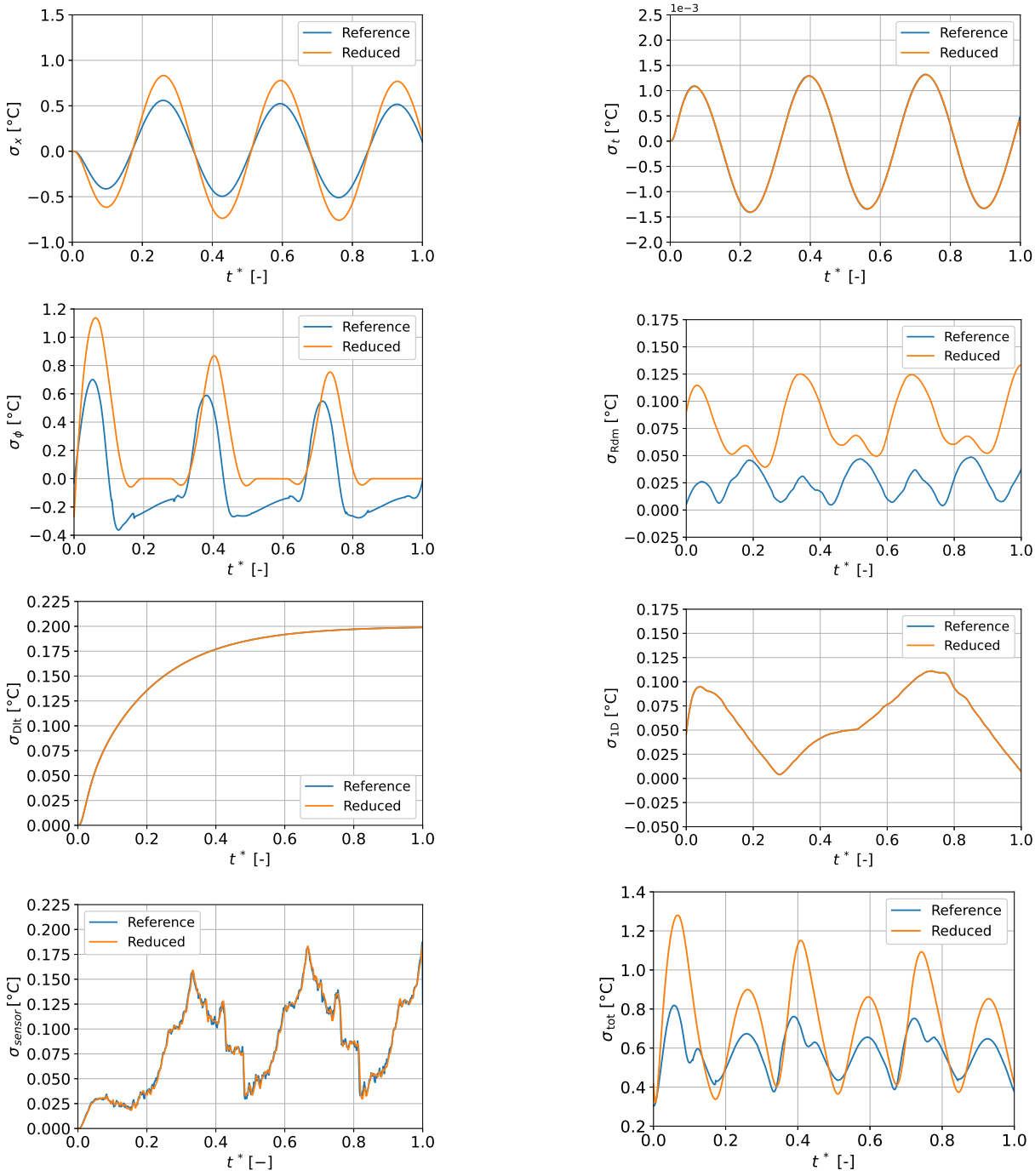

Figure 21. *Time variation of the uncertainties related to both reduced and reference configurations. Uncertainty due to (a) the sensor position, (b) its response time, (c) the mass transfer neglect, (d) the random aspect, (e)* Hypothesis 2 *and (f)* Hypothesis1*, (g) the sensor adherence rate to the sample surface. (h) Deduction of the entire uncertainty.*

We conclude that the total uncertainty of the reference case is oscillatory, almost periodic and varies between 0.4 and 0.8 °C. The reduced configuration is also approached in terms of uncertainties. As seen in Fig. 21, the order of magnitude of the calculated uncertainties remains the same. Nevertheless, there is a big difference between the reference and reduced configuration. σ_x, σ_ϕ and σ_{Rdm} are as important as we decrease the dimensions of the sample. Indeed, these uncertainties vary with the thickness of the sample.

They are small for thick materials, and large for a-thin ones. In this case, it is due to the magnitude of relative humidity and temperature gradients. It varies differently around the equivalent positions x_1 and x_2. They are more important in the reduced case. σ_t, σ_{Dlt} and σ_{Sensor} remain unchanged. Moreover, these do not depend on the factor of proportionality Σ, so increasing or decreasing the thickness of the sample does not influence these two uncertainties. Finally, the entire uncertainty is considerably greater than in the reference case. It reaches a maximum of 1.25 °C. Figs. 24(a) and 24(b) enable to visualize at two different time sequences the accumulated sub-uncertainty bands. Note that the magnitude of the entire uncertainty is not negligible. Consequently, it is necessary to carry out a calculation highlighting the propagation of uncertainties for the experimental results.

5.3.3 Discussion of validity of the thermal similarity

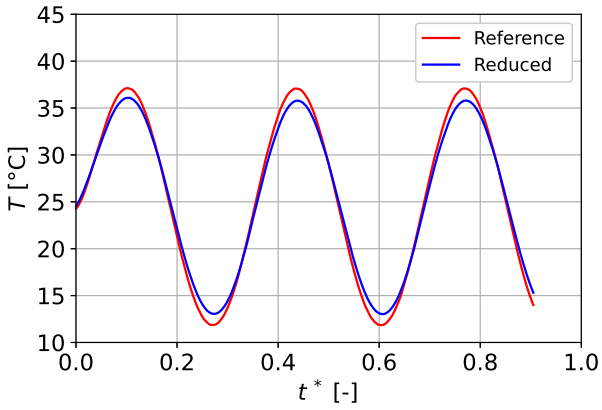

Figure 22. *Variation in temperature at* $x^\star = 0.5\,[-]$ *in the equivalent configurations.*

The parameters related to both tests and the boundary conditions (Fig. 20) were well defined in the previous section. The validity of the thermal similarity between the experimental results will be carried out on x_1 and x_2. The time variation in temperature at x_1 and x_2 in the dimensionless domain is shown in Fig. 22.

We have approximately a good agreement between the similar cases and note that both curves have the same shape. Nevertheless, there are instants where the discrepancy increases relatively. These moments correspond to the minimum or maximum air temperature. This difference in magnitude could be interpreted in several ways. The water content in the samples may not be the same. Indeed, the thermal conductivity increases with water content. In our case, the reference sample would be more humid, as it reaches greater limits than the one representing the reduced case. The micro-structure and the pore distribution may also be the source of these discrepancies. A more porous material has lower thermal conductivity due to the presence of air.

In order to include the calculated uncertainties in the experimental measurements, we focused more on sequences with a large discrepancy. This is illustrated in Fig. 23. It compares some experimental results while embedding the related entire uncertainties. The measurements are represented in a straight line. Moreover, the interval delimited by the dotted lines represents the range of the calculated entire uncertainty. During four different sequences, the uncertainty intervals for each configuration match within areas of different magnitudes.

Regarding both experiments, the discrepancy reaches a maximum of about 1.5 °C as shown in Fig. 25(a). On the other hand, the probability density shows a certain uniformity in the discrepancy distribution (Fig. 25(b)). The value 1.5 °C is largely justified by means of the calculated uncertainties $\sigma_{\mathsf{Tot}\,1}$ and $\sigma_{\mathsf{Tot}\,2}$. Indeed, $\sigma_{\mathsf{Tot}\,1} + \sigma_{\mathsf{Tot}\,2}$ is plotted with the discrepancy in the same Figure. Notice that the sum of both entire uncertainties is above the observed discrepancy most of the time. It ranges from 0.6 to 2 °C with an average of about 1.5 °C. (Fig. 25(b)).

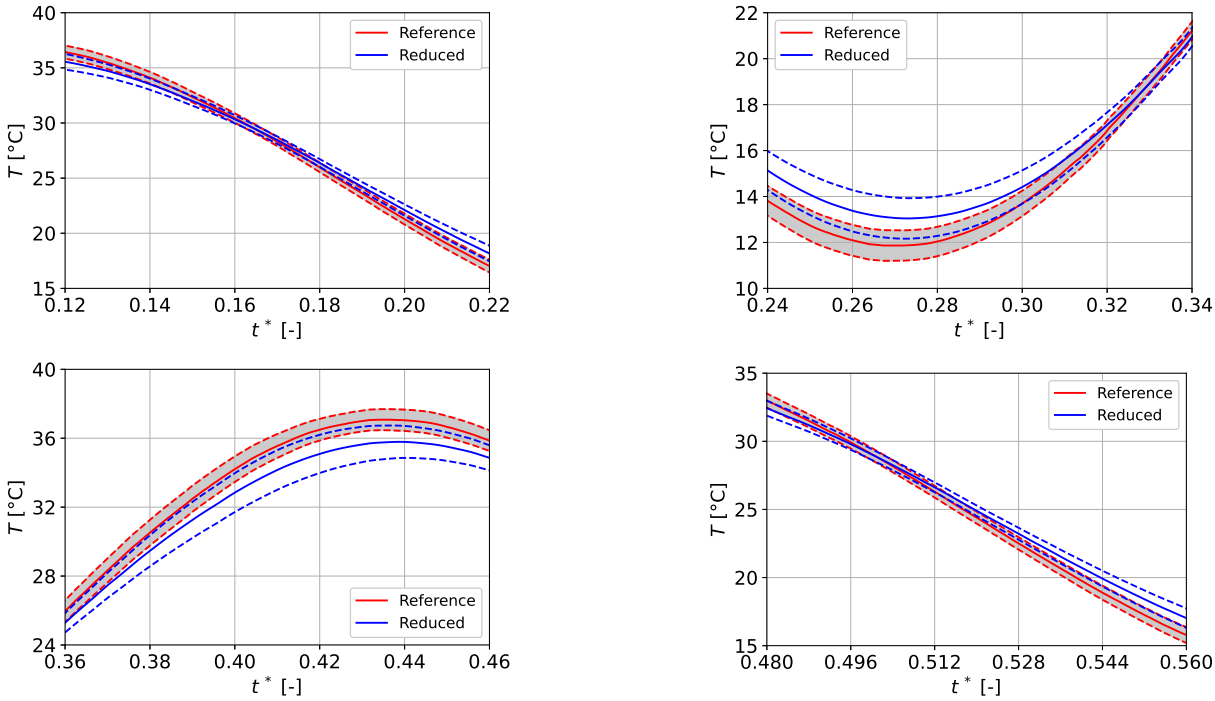

Figure 23. *Time variation in temperature at* $x^\star = 0.5\,[-]$ *during four different sequences. The dashed lines represent the entire uncertainties that correspond to each configuration.*

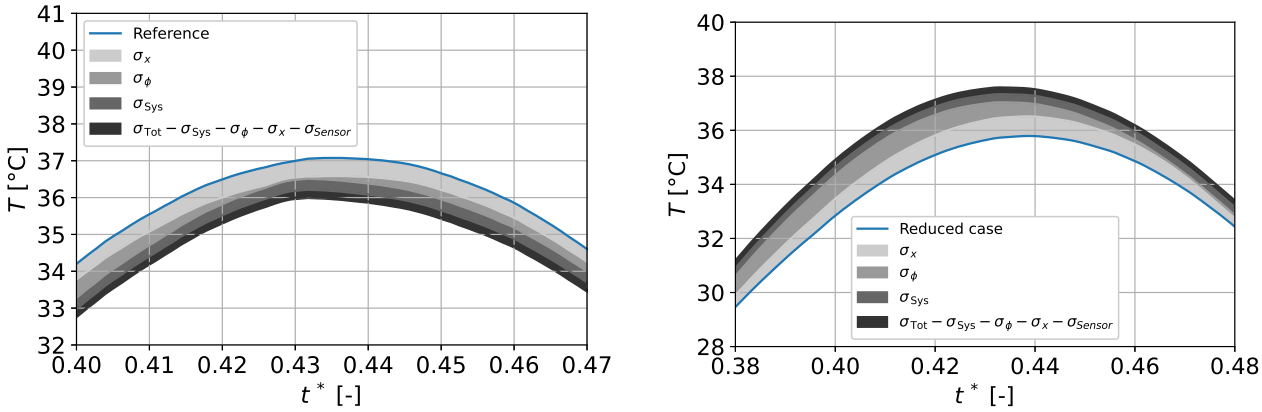

(a) (b)

Figure 24. *Temperature variation at two given time sequences for the reference case (a), and the reduced one (b) with the corresponding confidence intervals : sensor position* σ_x*, mass transfer influence* σ_ϕ*, sensor calibration* σ_{Sys} *and the remaining uncertainties* $\sigma_t + \sigma_{\text{Rdm}} + \sigma_{\text{Dlt}} + \sigma_{\text{1D}} + \sigma_{\text{Sensor}}$.

5.4 Discussion and further remarks

In order to carry out a similarity experiment, it is essential to control the conditions of equivalent configurations. The experimental results confirm the similarity law within a given margin of error (Fig. 22). Indeed, discrepancies during some sequences were observed. These instants correspond to large temperature gradients. Discrepancies result mainly from certain experimental imperfections. In this study, the use of similarity laws was limited to a one-dimensional heat transfer case using a thermal insulator. In a more general case, similarities could also be applied to a three-dimensional case. As an example, a non-insulated cubic sample exposed to a thermal stress, can be the basis of a similarity study. Indeed, the governing

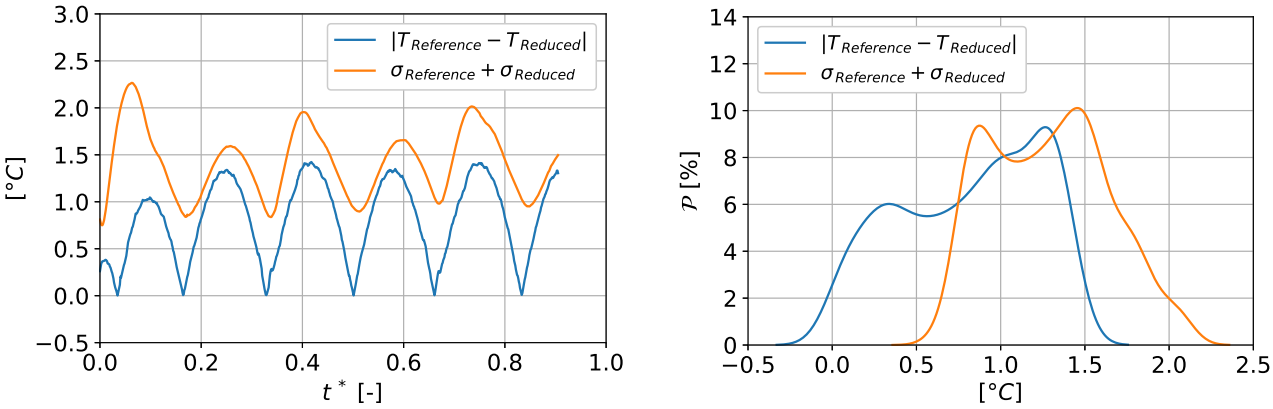

(a) (b)

Figure 25. *Temperature discrepancy and entire uncertainty between the configurations and the corresponding distributions*

equations and the dimensionless formulation are written this time according to three space dimensions L_x, L_y and L_z. As a result, the FOURIER number concept is extended. Thus, similarities between two different configurations are written according to Eq. (45):

$$\mathrm{Fo}_x^1 = \mathrm{Fo}_x^2\,, \quad \mathrm{Fo}_y^1 = \mathrm{Fo}_y^2\,, \quad \mathrm{Fo}_z^1 = \mathrm{Fo}_z^2\,. \tag{45}$$

where:

$$\mathrm{Fo}_\mathrm{x} = \frac{k_q^{ref}\, t_{ref}}{c_q^{ref}\, L_x^2}\,, \quad \mathrm{Fo}_\mathrm{y} = \frac{k_q^{ref}\, t_{ref}}{c_q^{ref}\, L_y^2}\,, \quad \mathrm{Fo}_\mathrm{z} = \frac{k_q^{ref}\, t_{ref}}{c_q^{ref}\, L_z^2}\,. \tag{46}$$

In addition, these laws can be applied to other types of boundary condition. In this study, the type Dirichlet was adopted to represent the conditions at the surface where $x = 0$. Dirichlet is the simplest type to model since temperature is assumed known at the surface. As for the Neumann type, an incident heat flux $\varphi\,[\mathrm{W.m^{-2}}]$ is considered. In this case, similarities involve, apart from FOURIER, a second dimensionless number, defined via Eq. (47):

$$\frac{\varphi^{ref}\, L}{k_q^{ref}\, T^{ref}}\,. \tag{47}$$

Regarding the ROBIN type, it represents the most realistic boundary condition. It involves two following parameters: air temperature and a surface heat exchange coefficient h_c. Similarities can also be applied in this case. If we ensure the same variation of air temperature in both configurations, then these laws can be expressed through Eq. (48) :

$$\mathrm{Fo}_q^1 = \mathrm{Fo}_q^2\,, \quad \mathrm{Bi}_q^1 = \mathrm{Bi}_q^2\,. \tag{48}$$

The BIOT number Bi involves h_c according to the following expression:

$$\mathrm{Bi}_q = \frac{h_c\, L}{k_q^{ref}}\,. \tag{49}$$

In this case, if we assume the use of the same material in similarity tests, thus resulting in $k_{q1}^{ref} = k_{q2}^{ref}$, we obtain the following result:

$$h_c^1 = h_c^2\, \Sigma\,, \quad \textit{where} \quad \Sigma = \frac{L_2}{L_1}. \tag{50}$$

Clearly, imposing a factor of proportionality such that $\Sigma \neq 1$ means that the experiments must be represented by two different thermal coefficients h_c^1 and h_c^2. In this respect, the knowledge of this coefficient

requires a complete characterization of the employed climate chamber, which leads to additional challenges. Indeed, the characterization depends on certain parameters such as the chamber size, air thermal properties as well as the flow velocity. Given that the chamber nor the fluid were changed, a variation of this coefficient could be caused only by an air velocity variation. It is therefore necessary to establish a law expressing h_c according to air velocity. Through this, it would be possible to fix the desired coefficient h_c by varying the flow velocity, which represents another challenge. Finally, this method would require a major investigation for cases considering a realistic boundary condition such as Robin.

Furthermore, there are uncertainties that can not be reduced. These are the ones related to the precision and response time of used equipment (sensors, measuring devices). There is also the random uncertainty which is due to the space variability of a material. In addition, the positioning of sensors induces also an unavoidable uncertainty that is proportional to the diameter of the sensor. On the other hand, other uncertainty sources can be controlled. In our case, they are the ones resulting from the three hypotheses initially set out. It was noticed that the effect of mass transfer on temperature is not quite negligible, and this was confirmed via the assessment of the uncertainty related to this hypothesis. The computation of this uncertainty was performed by means of Comsol Multiphysics. It is a numerical simulation software based on the finite element method. This software allows to simulate many physics and engineering applications, and especially coupled phenomena or multi-physics simulation. The last mentioned uncertainty was the predominant of the problem with values approaching $1\,°\mathsf{C}$. Therefore, it would be important to define similarities taking into account the coupling of heat and mass transfer phenomena. This also requires a good control of the material initial moisture state and moisture boundary conditions.

Due to the heterogeneity of the material, it was not that easy to overcome fully the uncertainty due to the one-dimensional transfer hypothesis. The heat flux is slightly smaller in the directions with more pores. Moreover, the presence of air decreases the thermal conductivity in these areas. Another important factor is the order of magnitude of the involved thermal conductivity. Indeed, the magnitude of this property is very similar between hemp concrete and polystyrene with the following values 0.100 and $0.032\,\mathsf{W.m^{-1}.K^{-1}}$. On the other hand, the uncertainty related to this hypothesis can be reduced by improving the insulation of the material. This uncertainty will persist unless one of the two following possibilities is verified experimentally. The thermal conductivity of the insulator equals zero. The second possibility requires the use of an insulator with an infinite thickness. With only $4\,\mathsf{cm}$, the one-dimensional transfer hypothesis was acceptable. The validation of the latter was based on a study which compared the real experimental approach and the lumped one representing a perfect one-dimensional case. In the above-mentioned investigations, analysis of temperature profiles was performed as well as the observed discrepancies. Heat maps and flux streamlines in experimental approach were discussed.

Moreover, it would be more appropriate to choose the right type of boundary conditions to better control similarity tests. Indeed, we emphasize that only air temperature is controlled in contrast to the one of the surface. Thus, we would not have necessarily a similarity in terms of surface temperatures, which is something that must be ensured. In order to control this temperature, suitable heating plates could be used, which adhere to the surface of the material. However, it would not be possible to vary it according to a variable time scenario. On the other hand, we ensure its perfect control. It would also be possible to use the Robin condition to control better climate scenario similarities, by varying the convective coefficient h_c in both configurations. This would be possible through the use of a climate chamber controlling not only air temperature and relative humidity, but also the flow rate of fans and thus the airflow velocity. Afterwards, similarity was established based on an additional assumption. It was assumed that the two samples used for tests have the same porosity. In reality, it was shown that hemp concrete has a porosity of about 72% [3]. Nevertheless, there is a margin of uncertainty related to this value. The latter can be estimated through reproducibility, which consists in evaluating the porosity of several samples issued from a same material. As a result, both samples have porosity around the mentioned value but slightly different. In this case, the heat transfer coefficient and density, which are directly correlated to porosity, are not exactly the same. Thus, it

would have been possible to include this additional source of uncertainty in this study, by carrying out an analysis of sensitivity regarding these two coefficients.

Lastly, when analyzing the literature, it was important to find studies where the validity of similarities had been investigated experimentally on a similar problem. A relevant study, that combined experimental (reduced configuration) and numerical approaches (real configuration), assessed the accuracy of these laws on a heat and mass transfer problem [27]. The real system corresponded to a multi-layer wall which was exposed to the climate stress of Tokyo during two years. Subsequently, this configuration was reduced by proposing 0.2 as factor of proportionality. The analysis of temperature results showed that both configurations led almost to equivalent variations. In this regard, results were satisfying with a maximum deviation of 1 °C. This discrepancy could be due to an uncertainty on both convective and radiation coefficients in the reduced configuration. In terms of comparison, there are some reasons that would not allow to confront correctly the results of this reference to those of our article. Differently from the heat equation, the model in [27] considers moreover the coupling with mass transfer, and water activity was the driving potential. Furthermore, the boundary conditions are not the same, i.e. the Robin type was adopted while considering convective and radiation effects. Finally, the nature of the materials constituted a third factor. Indeed, a composite material, highly heterogeneous and with high porosity was used in our study. Meanwhile, the mentioned research employed ordinary materials with medium porosity. In addition, it is worth noting that the heterogeneity of a material and its pore distribution can impact significantly the results of two similar configurations. In other words, the larger is the space variability of macroscopic properties, less identical are the material samples that are selected to carry out a similarity experiment.

6 Conclusion

The conclusions of the work are the following:

- Certain experimental protocols, related to transfer phenomena, entail a long period. These tests can last several months [8]. In order to address this problem and reduce the duration of experimental campaigns, the laws of similarity were used for a heat conduction problem. It enabled the reduction of a reference configuration by means of a reduced version. This study aimed to assess the validity of these laws through an experimental analysis. Based on similarities, an equivalent configuration was obtained verifying the factor of proportionality Σ. The duration of this configuration was therefore reduced by Σ^2. The one-dimensional transfer was ensured in both cases through the use of thermal insulation on the surrounding faces. Subsequently, the two configurations underwent similar thermal stress where both duration are proportional according to Σ^2.

- During both experiments, the aim was to measure and compare the temperature in equivalent positions. In order to discuss the validity of similarity, a complete evaluation of uncertainties was carried out. Uncertainties on sensor position, sensor response time, mass transfer effect, the systematic accuracy, the random aspect, the one dimensional transfer hypothesis, the modeling of a boundary condition and the one related to the adherence rate of a sensor were evaluated. The measurements in both configurations showed an acceptable agreement. The calculated discrepancy between equivalent fields of temperature reached 1.5 °C as a maximum value. It was often observed at instants corresponding to high air temperature gradients.

- In terms of uncertainties, the analysis showed that σ_x and σ_ϕ are the most preponderant ones. It was also demonstrated that the entire uncertainty is greater in the reduced configuration compared to the one in the reference. Finally, the time variation of both tests induced non negligible discrepancies

which were justified by means of entire uncertainties. Indeed, the sum of the latter for both configurations is much greater than the measured discrepancy.

- The validity of thermal similarities is relatively confirmed as long as the hypotheses of the model are well controlled. Furthermore, these laws could also be extended to the coupled heat and mass transfer model and be verified for both temperature and relative humidity fields. In this regard, an important assumption concerns the material properties. It is assumed that thermal conductivity and heat capacity do not change in both configurations. This assumption is acceptable for heat transfer properties but requires further investigation for coupled heat and mass transfer, particularly for building materials with complex micro-structures such as hemp concrete. For this reason, the extension of similarity for coupled heat and mass transfer in porous building material should be demonstrated.

Acknowledgements

The Region and the European Union support the project <CPER-FEDER Bâtiment durable Axis 2 MADUR Project: High-performance building materials with low environmental impact, sustainable and resilient> within the framework of the « Operational Program FEDER/FSE 2015-2020 and Energy saving certificate program of the Ministry of Ecological and Solidarity Transition "SmartReno support" 2019-2021.

References

[1] Matthaios Santamouris. *Energy Consumption and Environmental Quality of the Building Sector*. Elsevier Ltd, 2019. 1

[2] Ferhat Benmahiddine, Fares Bennai, Rachid Cherif, Rafik Belarbi, Abdelkader Tahakourt, and Kamilia Abahri. Experimental investigation on the influence of immersion/drying cycles on the hygrothermal and mechanical properties of hemp concrete. *Journal of Building Engineering*, 32(August):101758, 2020. 1, 20

[3] Ferhat Benmahiddine, Rachid Cherif, Fares Bennai, Rafik Belarbi, Abdelkader Tahakourt, and Kamilia Abahri. Effect of flax shives content and size on the hygrothermal and mechanical properties of flax concrete. *Construction and Building Materials*, 262:120077, 2020. 1, 7, 25

[4] S. Bahar Basturk, Claire E.J. Dancer, and Tony McNally. Jo ur na l P re. *Pharmacological Research*, page 104743, 2020. 1

[5] Nadjla Mostefai, Rabah Hamzaoui, Sofiane Guessasma, Amadou Aw, and Hedi Nouri. Microstructure and mechanical performance of modified hemp fibre and shiv mortars: Discovering the optimal formulation. *Materials and Design*, 84:359–371, 2015. 2

[6] Meijuan Rao, Mingxia Li, Huaquan Yang, Xiang Li, and Yun Dong. Effects of carbonation and freeze-thaw cycles on microstructure of concrete. *Journal Wuhan University of Technology, Materials Science Edition*, 31(5):1018–1025, 2016. 2

[7] B. Remki, K. Abahri, M. Tahlaiti, and R. Belarbi. Hygrothermal transfer in wood drying under the atmospheric pressure gradient. *International Journal of Thermal Sciences*, 57:135–141, 2012. 2

[8] A. Trabelsi, A. Belarbi, P. Turcry, K. Ait-Mokhtar. Water vapour desorption variability in situ concrete effects on drying, 2011. 2, 26

[9] N. Issaadi, A. A. Hamami, R. Belarbi, and A. Aït-Mokhtar. Experimental assessment of the spatial variability of porosity, permeability and sorption isotherms in an ordinary building concrete. *Heat and Mass Transfer/Waerme- und Stoffuebertragung*, 53(10):3037–3048, 2017. 2

[10] Abdelkrim Trabelsi, Zakaria Slimani, and Joseph Virgone. Response surface analysis of the dimensionless heat and mass transfer parameters of Medium Density Fiberboard. *International Journal of Heat and Mass Transfer*, 127:623–630, 2018. 2, 5

[11] Ramzy M. Abumandour, Islam M. Eldesoky, Mohamed H. Kamel, Mohamed M. Ahmed, and Sara I. Abdelsalam. Peristaltic thrusting of a thermal-viscosity nanofluid through a resilient vertical pipe. *Zeitschrift für Naturforschung A*, 75(8):727–738, 2020. 2

[12] Soliman R.El Koumy, El Sayed I. Barakat, and Sara I. Abdelsalam. Hall and Porous Boundaries Effects on Peristaltic Transport Through Porous Medium of a Maxwell Model. *Transport in Porous Media*, 94(3):643–658, 2012.

[13] Sara I. Abdelsalam and Abdullah Z. Zaher. Leveraging elasticity to uncover the role of rabinowitsch suspension through a wavelike conduit: Consolidated blood suspension application. *Mathematics*, 9(16), 2021. 2

[14] W. Neise. Application of Similarity Laws To the Blade Passage Sound of Centrifugal Fans. *Journal of Sound and Vibration*, 43:1975, 1975. 2, 6

[15] C. Codegone. A law of similarity for temperatures in enclosed turbulent flames. *Combustion and Flame*, 1(2):194–198, 1957. 2

[16] Leonardo M. Mazzariol and Marcílio Alves. Experimental verification of similarity laws for impacted structures made of different materials. *International Journal of Impact Engineering*, 133(April):103364, 2019. 2

[17] Sara I. Abdelsalam, Jorge X. Velasco-Hernández, and A. Z. Zaher. Electro-magnetically modulated self-propulsion of swimming sperms via cervical canal. *Biomechanics and Modeling in Mechanobiology*, 20(3):861–878, 2021. 2

[18] M. M. Bhatti and Sara I. Abdelsalam. Bio-inspired peristaltic propulsion of hybrid nanofluid flow with tantalum (ta) and gold (au) nanoparticles under magnetic effects. *Waves in Random and Complex Media*, 0(0):1–26, 2021.

[19] Kh.S. Mekheimer, R.E. Abo-Elkhair, S.I. Abdelsalam, Khalid K. Ali, and A.M.A. Moawad. Biomedical simulations of nanoparticles drug delivery to blood hemodynamics in diseased organs: Synovitis problem. *International Communications in Heat and Mass Transfer*, 130:105756, 2022. 2

[20] Subho Samanta and Abhijit Guha. A similarity theory for natural convection from a horizontal plate for prescribed heat flux or wall temperature. *International Journal of Heat and Mass Transfer*, 55(13-14):3857–3868, 2012. 2

[21] I. M. Eldesoky, Sara I. Abdelsalam, Wageeh A. El-Askary, and M. M. Ahmed. The integrated thermal effect in conjunction with slip conditions on peristaltically induced particle-fluid transport in a catheterized pipe. *Journal of Porous Media*, 23(7):695–713, 2020. 2

[22] Y Abd Elmaboud and Sara I Abdelsalam. DC/AC magnetohydrodynamic-micropump of a generalized burger's fluid in an annulus. *Physica Scripta*, 94(11):115209, aug 2019.

[23] M. M. Bhatti, Sultan Z. Alamri, R. Ellahi, and Sara I. Abdelsalam. Intra-uterine particle–fluid motion through a compliant asymmetric tapered channel with heat transfer. *Journal of Thermal Analysis and Calorimetry*, 144(6):2259–2267, 2021. 2

[24] Rabeeah Raza, Fazle Mabood, Rahila Naz, and Sara I. Abdelsalam. Thermal transport of radiative Williamson fluid over stretchable curved surface. *Thermal Science and Engineering Progress*, 23(February):100887, 2021. 2

[25] Menghao Qin, Rafik Belarbi, Abdelkarim Aït-Mokhtar, and Alain Seigneurin. An analytical method to calculate the coupled heat and moisture transfer in building materials. *International Communications in Heat and Mass Transfer*, 33(1):39–48, 2006. 2, 5

[26] Julien Berger, Clemence Legros, and Madina Abdykarim. Dimensionless formulation and similarity to assess the main phenomena of heat and mass transfer in building porous material. *Journal of Building Engineering*, 35(April 2020):101849, 2021. 2, 5

[27] Mamoru Matsumoto and Seiji Fujiwara. A study of annual moisture variation in an internally insulated building wall under a mild climate using a small-scale model and the similarity laws. *Energy and Buildings*, 16(3-4):933–945, 1991. 3, 26

[28] J. Michael Owen, Paul J. Newton, and Gary D. Lock. Transient heat transfer measurements using thermochromic liquid crystal. Part 2: Experimental uncertainties. *International Journal of Heat and Fluid Flow*, 24(1):23–28, 2003. 3

[29] Chong Wang and Hermann G. Matthies. Non-probabilistic interval process model and method for uncertainty analysis of transient heat transfer problem. *International Journal of Thermal Sciences*, 144(April):147–157, 2019. 3

[30] M. A.A. Mendes, S. Ray, J. M.C. Pereira, J. C.F. Pereira, and D. Trimis. Quantification of uncertainty propagation due to input parameters for simple heat transfer problems. *International Journal of Thermal Sciences*, 60:94–105, 2012. 3

[31] Chong Wang, Zhiping Qiu, and Yaowen Yang. Uncertainty propagation of heat conduction problem with multiple random inputs. *International Journal of Heat and Mass Transfer*, 99:95–101, 2016. 3

[32] Meicen Fan, Yue Chen, and Keshu Wan. Representative elementary volume analysis of hardened cement paste during hydration using X-ray Computed Tomography. *Construction and Building Materials*, 277:122268, 2021. 4

[33] I. M. Gitman, H. Askes, and L. J. Sluys. Representative volume: Existence and size determination. *Engineering Fracture Mechanics*, 74(16):2518–2534, 2007. 4

[34] B. A. Schrefler and Zhan Xiaoyong. A fully coupled model for water flow and airflow in deformable porous media. *Water Resources Research*, 29(1):155–167, 1993. 4

[35] J. Bear. Dynamics of fluids in porous media. *Soil Science*, 120:162–163, 1972. 4

[36] Francesco Goia, Gaurav Chaudhary, and Stefano Fantucci. Modelling and experimental validation of an algorithm for simulation of hysteresis effects in phase change materials for building components. *Energy and Buildings*, 174:54–67, 2018. 4

[37] Fang Liu, Binguang Jia, Baoming Chen, and Wenguang Geng. Moisture transfer in building envelope and influence on heat transfer. *Procedia Engineering*, 205:3654–3661, 2017. 4

[38] G. Gimenez, M. Errera, D. Baillis, Y. Smith, and F. Pardo. A coupling numerical methodology for weakly transient conjugate heat transfer problems. *International Journal of Heat and Mass Transfer*, 97:975–989, 2016. 4

[39] Sahar Hamidi, Thomas Heinze, Boris Galvan, and Stephen Miller. Critical review of the local thermal equilibrium assumption in heterogeneous porous media: Dependence on permeability and porosity contrasts. *Applied Thermal Engineering*, 147(October 2018):962–971, 2019. 5

[40] J. Lévêque and A. Rezzoug. Dimensionless and analytical studies of the thermal stability of a high temperature superconducting tube. *International Journal of Heat and Mass Transfer*, 48(14):2815–2821, 2005. 5

[41] L. M. Biberman, S. Ya Bronin, and A. N. Lagar'kov. Radiative and convective heat transfer in hypersonic flow around a blunt body. *Fluid Dynamics*, 7(5):800–809, 1972. 6

[42] H. J. Kaeppeler and N. Ruhs. Similarity laws in turbulent focus plasma with beam-beam neutron production. *Physics Letters A*, 49(5):383–385, 1974. 6

[43] John R Taylor. [John_R._Taylor]_An_Introduction_to_Error_Analysis(BookZZ.org).pdf, 1997. 10, 12

[44] Julien Berger, Thomas Busser, Sohail Reddy, and George S. Dulikravich. Evaluation of the reliability of a heat and mass transfer model in hygroscopic material. *International Journal of Heat and Mass Transfer*, 142:118258, 2019. 11, 20

[45] Merlin Simo-Tagne, Romain Rémond, Yann Rogaume, André Zoulalian, and Beguide Bonoma. Modeling of coupled heat and mass transfer during drying of tropical woods. *International Journal of Thermal Sciences*, 109:299–308, 2016. 11

[46] Hartwig M. Künzel and Kurt Kiessl. Calculation of heat and moisture transfer in exposed building components, 1996. 11

[47] Mohammed Yacine Ferroukhi, Rafik Belarbi, Karim Limam, and Walter Bosschaerts. Impact of Coupled Heat and Moisture Transfer. *Thermal Science*, 21(3):1359–1368, 2017.

[48] Suelen Gasparin, Julien Berger, Denys Dutykh, and Nathan Mendes. An adaptive simulation of nonlinear heat and moisture transfer as a boundary value problem. *International Journal of Thermal Sciences*, 133(July):120–139, 2018. 11